Efficient Modeling of Hybrid-Electric Aircraft for Design and Performance Optimization Studies

H. Tran

Technische Universiteit Delft

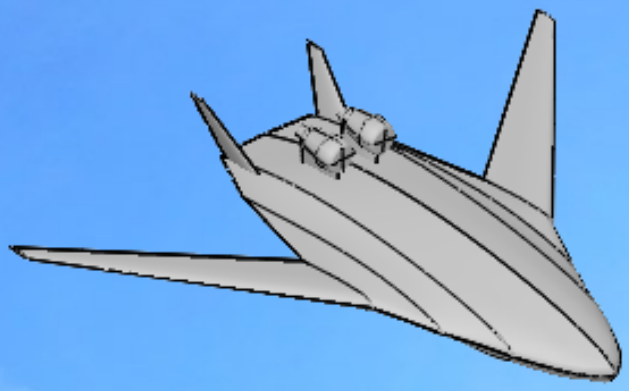

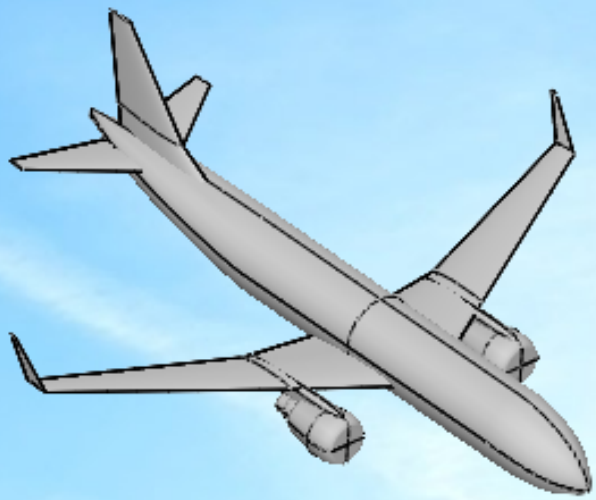

TU Delft Delft University of Technology

nlr

Challenge the future

Efficient Modeling of Hybrid-Electric Aircraft for Design and Performance Optimization Studies

by

H. Tran

in partial fulfillment of the requirements for the degree of

Master of Science
in Aerospace Engineering

at the Delft University of Technology,
to be defended publicly on Tuesday December 15, 2020 at 12:30 PM.

Student number:	4345371	
Project duration:	December 2, 2019 – December 15, 2020	
Supervisor:	Ir. J. Melkert,	TU Delft
Thesis committee:	Ir. J. Melkert,	TU Delft
	Dr. ir. J. Vankan,	NLR
	Dr. ir. G. La Rocca,	TU Delft
	Ir. P.C. Roling,	TU Delft

An electronic version of this thesis is available at http://repository.tudelft.nl/.
Number of equivalent words: 19,781

TU Delft Delft University of Technology

Preface

This thesis is the final piece that is written to complete my studies in Aerospace Engineering at Delft University of Technology (TU Delft). During my internship at the Netherlands Aerospace Centre (NLR), the research topic arose when I was discussing with my colleagues. I was thrilled to hear that I could perform research on this interesting topic for both NLR and TU Delft.

I would like to express my gratitude to my supervisors Joris Melkert and Jos Vankan for their relentless support and invaluable feedback. Every moment I have spent with them have created learning opportunities and led to new insights. I am also grateful to Wim Lammen for providing help whenever I felt lost during the thesis. Furthermore, I would like to give my thanks to Gianfranco La Rocca and Paul Roling for assessing my work. I would also like to thank my fellow graduation interns at NLR for the fun moments and help: Arnault-Quentin, Assia, Robin, Sébastien, Gigi, Beau, and George. Last but not least, I would like to thank my sister and parents for their care and encouragement.

H. Tran
Delft, December 2020

Summary

The world is faced with two concurrent trends. The first is the growing demand for air travel in the long term. The second is the need to cut aircraft emissions due to environmental goals and ambitions set by authorities. Fully-electric aircraft are currently infeasible due to the limited battery specific energy and power. Hybrid-electric propulsion (HEP) technology offers an intermediate solution. HEP can work in tandem with new aircraft designs, which potentially leads to further reductions in fuel and energy consumption. This study aims to quantify those reductions.

A parallel HEP aircraft mission simulation framework 'MASS' has been developed at Netherlands Aerospace Centre. Earlier studies with MASS have pointed out that HEP retrofit aircraft have the potential to reduce fuel consumption. The expectation is that even more fuel can be saved by varying the HEP parameters and airframe geometry together. Hence, this study focuses on extending MASS to incorporate new aircraft designs.

The extension is made in Matlab and involves adding the capability to calculate aircraft level aerodynamics and weight based on the geometry. A tool called 'OpenVSP' is used to generate the aircraft geometry. Then, the aircraft drag polar is constructed using a combination of the aerodynamic solver 'VSPAero' and handbook methods. Maximum deviation between predicted and actual drag for the relevant lift coefficients is 7.3%. The weight is calculated using Class-II estimation methods. Two separate sets of formulae are used: One is meant for the tube-and-wing (TAW) configuration whereas the other is dedicated to blended wing-body (BWB). The predicted operational empty mass deviates less than 1% from the reference for TAW aircraft, and 2.3% for BWB.

HEP-related research is currently focused on large passenger aircraft. In this study an A320neo aircraft is used as reference aircraft, which is parallel HEP retrofitted. It is subjected to hybrid-electric powertrain and geometry variations in order to quantify the potential fuel burn reductions. During the variation studies, the same mission of 800 nm and 150 pax is simulated. The selected powertrain design variables are the engine core scaling and the power split. The latter is the electric power provided by the batteries to the engine, divided by the total amount of power. The idea of using the power split is to support the downscaled engine core during high thrust phases, which would otherwise not have enough power.

A design of experiments is conducted prior to the unconstrained optimization for minimal fuel burn. The optimization is performed directly using Matlab function 'fmincon'. The powertrain optimum shows a 3.1% fuel burn reduction. The geometry variation is done in two ways: one involves planform changes and the other a configuration change to BWB. The optimization with powertrain and planform variables is done via a surrogate model obtained using an artificial neural network. The optimum shows a 16.9% reduction in fuel burn, where the planform contributes more to the reduction than the powertrain.

For the BWB fuel burn quantification the same process is applied. The powertrain optimization shows a 3% fuel burn reduction with respect to its non-HEP variant. A 13.8% fuel reduction is obtained with powertrain and planform variations. Again, the planform is a larger determinant of fuel burn reduction than the powertrain. Compared with the non-HEP A320neo, a maximum of 19.9% fuel burn reduction can be achieved.

Contents

List of Figures

List of Tables

Nomenclature

Latin Symbols

A	Aspect ratio	$-$
b	Wing span	m
c	Chord length	m
c	Factor	$-$
C_D	Drag coefficient	$-$
C_d	2D drag coefficient	$-$
C_f	Friction coefficient	$-$
C_L	Lift coefficient	$-$
C_l	2D lift coefficient	$-$
C_M	Moment coefficient	$-$
D	Drag	N
d	Diameter	m
e	Specific energy	Wh/kg
FF	Form factor	$-$
h	Altitude	m
i	Incidence angle	deg
k	Factor	$-$
K_y	Pitching radius of gyration	m
L	Lift	N
l	Length	m
M	Mach number	$-$
M	Moment	Nm
m	Mass	kg
MLW	Maximum Landing Weight	kg
$MTOM$	Maximum Take-Off Mass	kg
$MTOW$	Maximum Take-Off Weight	kg
$MZFW$	Maximum Zero Fuel Weight	kg
N	Amount of	$-$
n	Amount	$-$
n	Load factor	$-$
OEW	Operational Empty Weight	kg
p	P-statistic	$-$
p	Specific power	kW/kg
pax	Amount of passengers	$-$
Q	Interference factor	$-$
R	Correlation coefficient	$-$
R	Range	nm
r	Radial distance	$-$
Re	Reynolds number	$-$
S	Surface area	m^2
s	Distance	m
s	Scaling factor	$-$
T	Thrust	N
t	Thickness	m
V	Volume	m^3
V_D	Dive speed	m/s
W	Weight	kg
w	Width	m
x	X-coordinate	$-$
Y	Side force	N
y	Y-coordinate	$-$
z	Z-coordinate	$-$

Greek Symbols

α	Angle of attack	deg
α	Wing-fuselage intersection angle	rad
η	Efficiency	$-$
Γ	Circulation	m^2/s
Γ	Dihedral angle	deg
κ_A	Korn factor	$-$
Λ	Sweep angle	deg

λ	Taper ratio	$-$
ϕ	Degree of hybridization	$-$
ϕ	Wake potential increment	m^2/s
ϕ	Wing-fuselage intersection angle	rad
ϕ_e	Hybridization factor	$-$
ϕ_p	Power split	$-$
ρ	Density	kg/m^3
θ	Inclination angle	rad

Subscripts

bat	Battery
cl	Climb
cr	Cruise
D	Design
DD	Drag divergence
de	Design empty
des	Design
dg	Design gross
e	Elevator
e	Energy
e	Engine on fuselage penalty
el	Electrical system
EM	Electric Motor
en	Engine
f	Fuel
fus	Fuselage
h	Horizontal tail
$htail$	Horizontal tail
i	Induced
i	Inner
$interf$	Interference
k	Kink
L	Landing
lav	Lavatory
MO	Maximum Operating
o	Outer
OE	Operational empty
p	Power
p	Pressurization
par	Parasite
$pass$	Passenger
PL	Payload
r	Root
re	Engine on wing penalty
ref	Reference
SL	Sea-level
sl	Slat
sp	Spoiler
t	Tip
TO	Take-off
tot	Total
uc	Undercarriage
uht	All-moving horizontal tail
ult	Ultimate
v	Vertical tail
w	Wing
w	Winglet
wl	Winglet

List of Abbreviations

ACARE	Advisory Council for Aviation Research and Innovation in Europe
ANN	Artificial neural network
APU	Auxiliary power unit
ATR	Aerei da Trasporto Regionale
BLI	Boundary layer ingestion
BWB	Blended Wing-Body
ceo	Current engine option
CeRAS	Central Reference Aircraft data System
CFD	Computational fluid dynamics
CG	Center of gravity
CSR	CeRAS short range reference aircraft
DP	Distributed propulsion
DRAGON	Distributed fans Research Aircraft with electric Generators by ONERA
EFTA	European Free Trade Association
EIS	Entry into service
EU28	28 countries of the European Union
GA	General Aviation
GUI	Graphical user interface
HEA	Hybrid-electric aircraft
HEP	Hybrid-electric propulsion
HEPS	Hybrid-electric propulsion system
IATA	International Air Transport Association
LEAP	Leading Edge Aviation Propulsion
LHS	Latin hypercube sampling
LPA	Large Passenger Aircraft
MASS	Mission Aircraft and Systems Simulation for HEP performance analysis
MDAO	Multidisciplinary Design, Analysis and Optimization
MTOW	Maximum Take-Off Weight
MICADO	Multidisciplinary Integrated Conceptual Aircraft Design and Optimization Environment
NACA	National Advisory Committee for Aeronautics
NASA	National Aeronautics and Space Administration
neo	New engine option
NLR	Netherlands Aerospace Centre
OEW	Operational empty weight
ONERA	French Aerospace Lab/Office National d'Etudes et de Recherches Aérospatiales

OpenVSP	Open Vehicle Sketch Pad
PEGASUS	Parallel Electric Gas Architecture with Synergistic Utilization Scheme
PHEP	Parallel hybrid-electric propulsion
RANS	Reynolds-averaged Navier-Stokes
RBF	Radial basis function
RWTH Aachen	Rheinisch-Westfälische Technische Hochschule Aachen
SIP	Strategic implementation plan
SRIA	Strategic research and innovation agenda
SUAVE	Stanford University Aerospace Vehicle Environment
SUGAR	Subsonic Ultragreen Aircraft Research
TAW	Tube-and-wing
TBW	Truss-braced wing
TL	Technology level
TLAR	Top level aircraft requirements
TU Delft	Delft University of Technology
VLM	Vortex lattice method

1

Introduction

The need for improved efficiency of aircraft propulsion systems stems from the growing demand in air travel and at the same time the ambitious targets for reducing aviation emissions. As predicted in the European aviation environmental report from 2019 [19], the number of flights to or from EU28 and European Free Trade Association (EFTA) airports is expected to grow from 9.56 million in 2017 to 13.6 million in 2040. Globally, IATA[1] predicts an annual increase of 3.5% of air traffic for the coming 17 years. From a manufacturer's perspective, Airbus anticipates more than double the current traffic of their own fleet in the 15 years to come, which conforms with the growth of 140% since the year 2000 [1]. Both Airbus and Boeing predict their fleet to grow more than double by 2038 as evident in Figures 1.1 and 1.2 respectively.

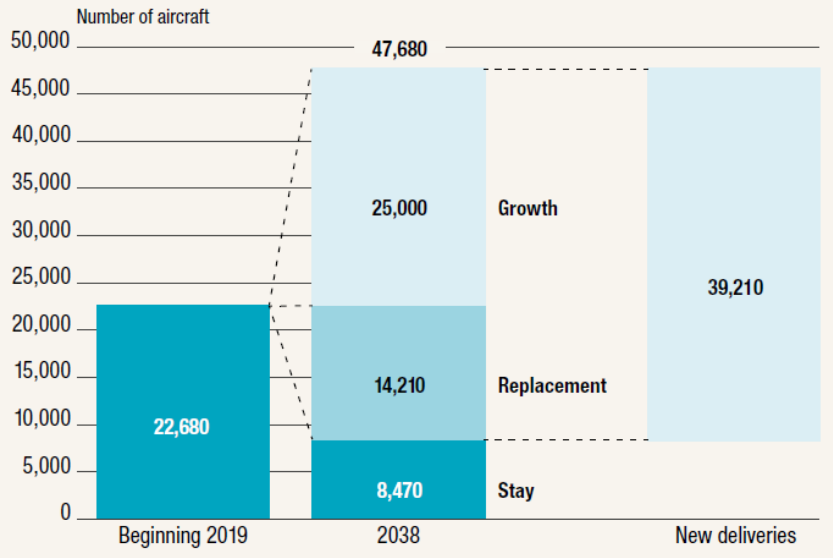

Figure 1.1: Predicted fleet growth of Airbus [1].

Besides the increasing air traffic in the near future, new goals and ambitions are set by various stakeholders in the aviation industry, in order to mitigate the environmental ramifications of air travel. The European Commission created their vision for aviation in 2050, referred to as 'Flightpath 2050', which entails many ambitious goals including a 75% reduction in CO_2 emissions per pax/km and 90% reduction in NO_x compared to typical new aircraft from 2000 [20]. It contributes to a 90% reduction in greenhouse gases by 2050, shared by all means of transportation as imposed by the European Green Deal[2]. NASA developed their environmental targets for aviation in similar fashion as part of

[1] https://www.iata.org/en/pressroom/pr/2018-10-24-02/, visited on 21/4/2020

[2] https://ec.europa.eu/info/sites/info/files/european-green-deal-communication_en.pdf, visited on 21/4/2020

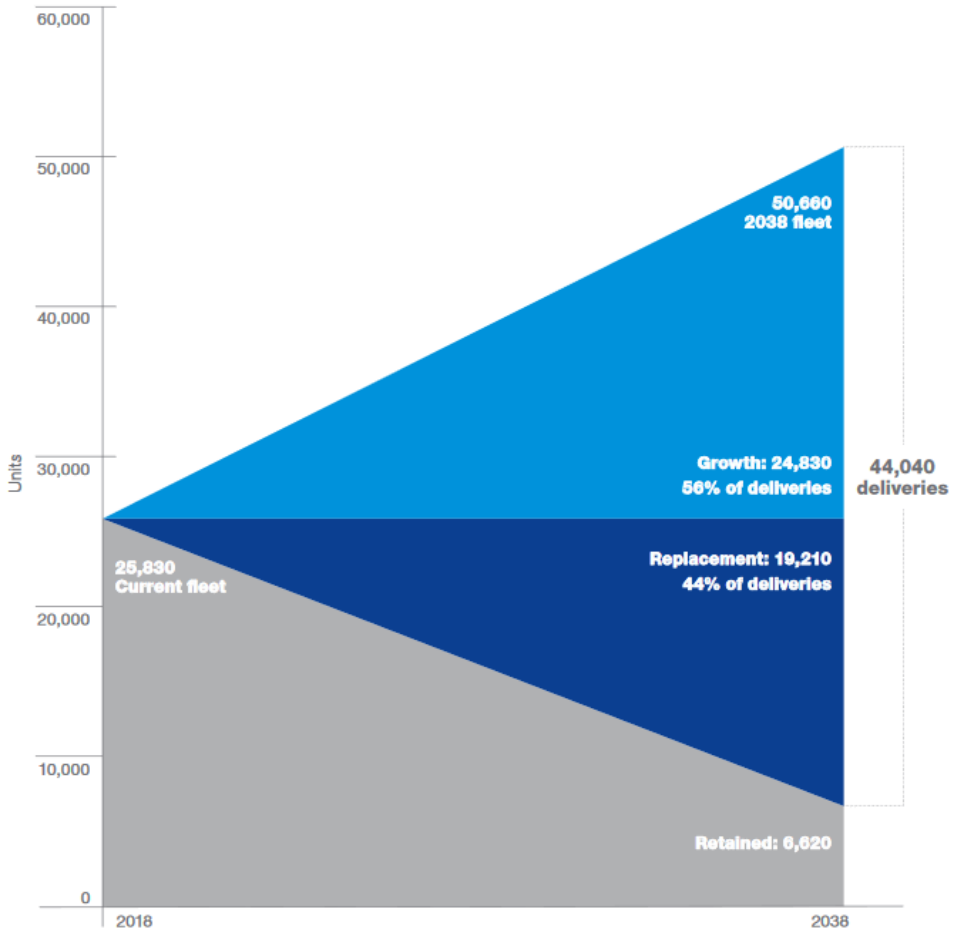

Figure 1.2: Predicted fleet growth of Boeing [2].

the Strategic Implementation Plan (SIP) [21]. Furthermore, the Advisory Council for Aviation Research and Innovation in Europe (ACARE) discusses and states action points under their strategic research and innovation agenda (SRIA) to tackle each of the goals from Flightpath 2050. Regarding the environment, SRIA's challenge of 'protecting the environment and the energy supply' is accompanied by one of its action points urging to 'develop air vehicles of the future: revolutionary steps' [22]. A technology with potential benefit to this action point is Hybrid Electric Propulsion (HEP), which is part of current research dedicated to aircraft with entry into service (EIS) in 2035. In HEP, a conventional propulsion system is supported by an additional electric energy/power source. More information on HEP definitions and architectures is provided in Section 1.1. In recent years there has been a surge in hybrid-electric aircraft (HEA) related research [11]. The introduction of HEP architectures has led to new conceptual aircraft configurations as seen in Fig. 1.3.

The list in Figure 1.3 can be expanded with NASA's Parallel Electric-Gas Architecture with Synergistic Utilization Scheme (PEGASUS) HEA concept that is based on an ATR 42-500 [4], see Figure 1.4. It features BLI and a four-engine configuration. Its wingtip propulsors are sized for cruise. The inboard propellers are foldable and only meant for assisting in take-off, climb, and one-engine-inoperative conditions.

Further expansion of the list is made with ONERA's DRAGON (see Figure 1.5) [5] that is part of Europe's Clean Sky 2 program. This hybrid-electric distributed propulsion concept for EIS 2035 has similar TLAR as an A320ceo, such as a cruise Mach of 0.78, 2750 nm range, and 150 pax.

It can be seen that the HEP research trend shifted from application to General Aviation (GA) to Large Passenger Aircraft (LPA). The trend nowadays is focused on aircraft HEP retrofit studies and unconventional configurations that are made in tandem with HEP technology. The newer aircraft concepts are characterized by one or a combination of the following features:

Figure 1.3: A subset of electrified aircraft concepts for entry into service from 2030 onward [3].

Figure 1.4: NASA's PEGASUS concept: a retrofitted ATR 42-500 using wingtip propulsors and BLI [4].

Figure 1.5: ONERA's hybrid-electric DRAGON concept [5].

- Aircraft propulsion system variations:
  - HEP retrofit
  - Wingtip propulsion
  - Boundary Layer Ingestion (BLI)
  - Distributed propulsion (DP)
- Airframe variations:
  - Non-planar wings
  - Blended Wing-Body (BWB)

– Truss-braced wings

Table 1.1 presents some numbers on the fuel saving benefits of various HEA concepts. The fuel savings are compared with their respective conventional counterpart.

Table 1.1: Numbers on fuel savings of various HEA concepts. [10, 11]

Aircraft	**Highlights**	**EIS year**	**Fuel burn change [%]**	**Source**
Boeing SUGAR Volt	TBW, PHEP	2035	-10.9%	[23]
A320 PHEP retrofit	PHEP	2035	-7%	[6]
PEGASUS	BLI, PHEP, wingtip propulsors	2030	-42%	[4]
DRAGON	HEP, DP	2040	-7%	[5]
VJB Single-Aisle	VJB, SPPH	2035	-15%	[24]
A320 equivalent LPA	HEP BLI-Canard	2035	-3%	[25]
ATR-72-600 retrofit	PHEP	2035	-28%	[26]

The quantification of the effects on fuel burn of each individual variation is not always clear since usually concepts are assessed as a whole. Moreover, purely adding one element such as HEP may result in a slight redesign of the aircraft to cope with the added weight, for instance. The ATR-72-600 HEP retrofit study by Voskuijl et al. [26] is an example of that. However, certain elements have been found to be treated separately in other studies. For instance, Boeing's truss-braced wing concept is predicted to reduce up to 53.6% block fuel w.r.t. its reference design [23]. The parallel HEP powertrain retrofit applied to that led to another 10.9% reduction.

Many different concepts have been analyzed over the years, but were all subjected to different and often proprietary tools and methods. This renders it difficult to compare those results on aircraft level [27]. Examples of frameworks for analysis of (hybrid-electric) aircraft are: MICADO developed by RWTH Aachen University [27], GT-HEAT by Georgia Tech [28], PANTHER by ESAero[3], MASS by NLR [29], Initiator by TU Delft [30], SUAVE by Stanford University [31]. However, as Brelje and Martins [10] have identified, the full Multidisciplinary Design Analysis and Optimization (MDAO) of HEA has not been addressed yet.

At Netherlands Aerospace Centre (NLR), studies have been performed on aircraft propulsion hybridization which have led to the development of a multidisciplinary analysis and optimization framework called MASS (Mission Aircraft and Systems Simulation for HEP performance analysis). Figure 1.6 shows a schematic overview of the modules of MASS and their interrelationship.

[3]https://www.esaero.com/expertise.html, visited on 9 April 2020.

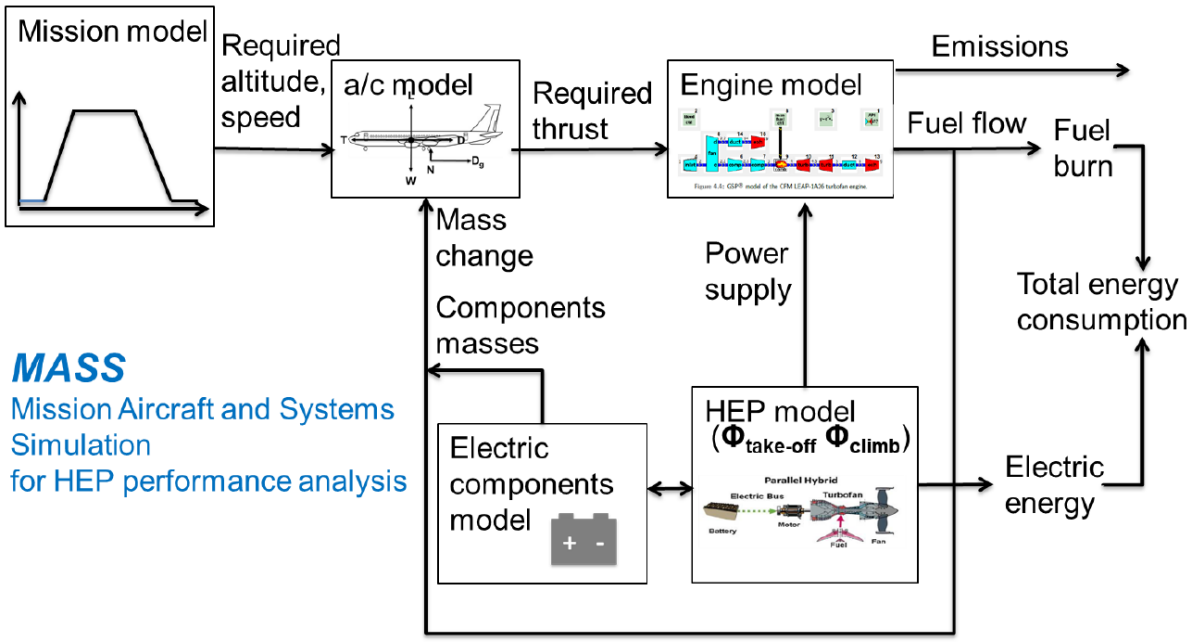

Figure 1.6: MASS framework schematic [6].

In 2016, research was conducted on the power management strategy of a hybrid-electric propulsion system (HEPS) to improve fuel economy using integrated aircraft performance and propulsion models [32], based on an A320neo. A subsequent study adds knowledge about the effects on fuel and energy consumption by implementing electrified non-propulsive systems, photovoltaics, fuel cells, and engine scaling [33]. A more recent paper describes the study on fuel and energy consumption of a HEP retrofitted A320neo [29]. Follow-up papers have added the knowledge about the effect of mission parameter variations (range, speed, and pax) [34], and the potential energy and fuel savings for energy optimized take-off and climb hybridization factors and engine scaling [6]. The studies performed so far involve powertrain variations, but more fuel savings are expected if geometry variations are included. In fact, MASS has been mainly applied to one aircraft model, the A320neo. Since the overall HEP research encompasses a variety of aircraft configurations and technologies [35], the subject of this research is to enhance the flexibility of the current framework.

1.1. Hybrid-Electric Propulsion

This section provides more information on the definitions used regarding hybrid-electric propulsion in aircraft.

Degree of Hybridization

Aircraft can be characterized by their degree of hybridization, which is a non-dimensional quantity denoted by ϕ. In the context of hybrid-electric aircraft, the degree of hybridization is related to energy (ϕ_e) and power (ϕ_p). ϕ_e is defined as the ratio between the amount of stored electrical energy in batteries, E_b, and the total amount of energy (fuel plus electric) carried for the mission, E_{tot} [10] (Equation 1.1). Although it had different definitions over the years [36], for this study ϕ_e is referred to as the 'degree-of-hybridization for block energy' [37] or the hybridization factor [26]. ϕ_p is defined as the ratio between the amount of power provided by the electric motor, P_{EM}, divided by the total shaft power, P_{tot} (Equation 1.2). The term 'power split' is used for ϕ_p.

$$\phi_e = \frac{E_b}{E_{tot}} \tag{1.1}$$

$$\phi_p = \frac{P_{EM}}{P_{tot}} \tag{1.2}$$

Hybrid-Electric Propulsion Architectures

The definitions of ϕ_e and ϕ_p (Equations 1.1 and 1.2 respectively) imply that conventional, fully fuel-based aircraft have $\phi_e = \phi_p = 0$, whereas fully-electric aircraft have $\phi_e = \phi_p = 1$. In turbo-electric aircraft, there are no batteries for energy storage, but there is electrical power transmission between the turbine and driveshaft. Hence that in that case $\phi_e = 0$, $\phi_p > 0$ [10]. Hybrid-electric architectures are characterized by $0 < \phi_e, \phi_p < 1$ [10], and are globally divided into serial and parallel configurations [38]. A more detailed schematic overview of HEP architectures is depicted in Figure 1.7. In series HEP all propulsors are driven by electric motors, but the energy comes from both batteries and fuel combustion, resulting in $\phi_p = 1$ and $\phi_e > 0$. In parallel HEP aircraft, propulsors are driven by electric motors and combustion engines, resulting in $\phi_p < 1$ and $0 < \phi_e < 1$. In summary, Table 1.2 provides an overview of the architectures together with ϕ_e and ϕ_p.

Table 1.2: Aircraft propulsion architectures categorized by degree-of-hybridization ϕ_e and power split ϕ_p.

Architecture	ϕ_e	ϕ_p
Conventional	0	0
Turbo-electric	0	(0, 1]
Series hybrid-electric	(0, 1]	1
Parallel hybrid-electric	(0, 1)	[0, 1)
Fully-electric	1	1

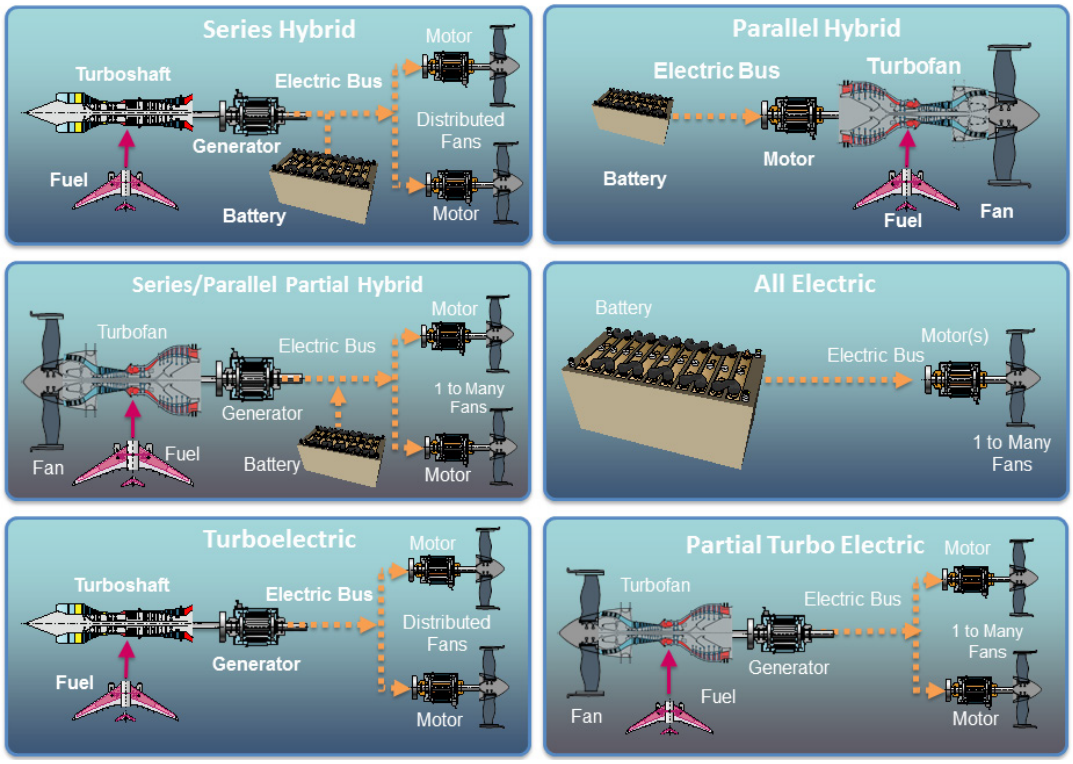

Figure 1.7: Schematic drawings of electrified aircraft propulsion architectures [7].

2

Research Plan

The aim of this chapter is to provide details on the research project. The research questions and objectives and the employed methodology are explained. Major milestones are presented and in addition, the accompanying Gantt chart is depicted in Appendix A.

2.1. Research Objective and Questions

The main objective of this research is:

> "... to quantify the potential reductions in trip fuel that can be achieved with hybrid-electric aircraft (HEA) by aircraft concept variations using a to be developed extension of the current multidisciplinary analysis and optimization framework for HEA developed by NLR."

The accompanying research questions are as follows:

1. What are the achievable fuel and energy reductions of hybrid-electric aircraft (HEA) at their expected year of entry in service (2035) compared to their conventional counterparts?
   (a) What HEA technologies are envisaged for use by the year 2035?
   (b) How are fuel and energy consumption of HEA calculated?
   (c) Which conventional aircraft are suitable as reference, regarding the availability of their verification and validation data?
   (d) What HEA sizing parameters are the main determinants for trip fuel and energy savings?
2. Which aircraft design disciplines are the most relevant for the current multidisciplinary analysis and optimization framework for HEA?
   (a) Which aircraft design disciplines are relevant for analysis of HEA?
   (b) What are the strengths and weaknesses of the framework?
   (c) What aircraft design elements and methods are to be implemented in the framework?

2.2. Research Methodology and Scope

This research is conducted at Netherlands Aerospace Centre (NLR) and Delft University of Technology (TU Delft).

The result of this research shall be the extended MASS framework that is capable of assessing fuel and energy consumption of HEA aircraft for a broader range of aircraft configurations. The idea is to obtain indicative values for conventional as well as unconventional aircraft designs with similar TLAR. The current research trend is focused on LPA category aircraft, to which the A320neo belongs. Due to data availability and common use of this aircraft, it will serve as this study's main aircraft. The first step of the research is to split the framework extension into three subjects: geometry modeling, aerodynamic modeling, and weight estimation. The geometry model includes aircraft parameterization

and visualization. Ideally it shall allow for the creation of arbitrary aircraft configurations and sizes, but this study is only limited to LPA. It also serves as input for aerodynamic and weight calculations. Due to the point-mass aircraft representation in MASS, is it required to obtain aircraft-level aerodynamic results such as the drag polar. The weight estimation shall be detailed enough to capture the effects of changing geometry.

2.3. Research Planning

The research duration is 12 months, including the courses AE4010 Research Methodologies and AE4020 Literature Study. The Gantt chart is inserted in Appendix A. The milestones are listed below for reference:

- Thesis kick-off - 2 December 2019
- Hand-in research methodology report - 31 January 2020
- Literature study presentation - 1 May 2020
- Mid-Term review - 25 May 2020
- Green light review - 19 October 2020
- Thesis defence - 15 December 2020

3

Framework Extension

This chapter is dedicated to the theory and implementation of the aircraft design module that is used to extend the MASS framework. The main idea is to obtain a drag polar for any clean aircraft configuration. That is then used for mission simulations with a point-mass aircraft representation. The extension consists of the modeling of the aircraft's geometry and the aerodynamic analysis. A general overview of the workflow is given in Figure 3.1. The working sequence is to generate the aircraft geometry first, as described in Section 3.1. Subsequently, aerodynamic analysis is performed on the input geometry, as described in Section 3.2. The validation of the method is explained in Section 3.3.

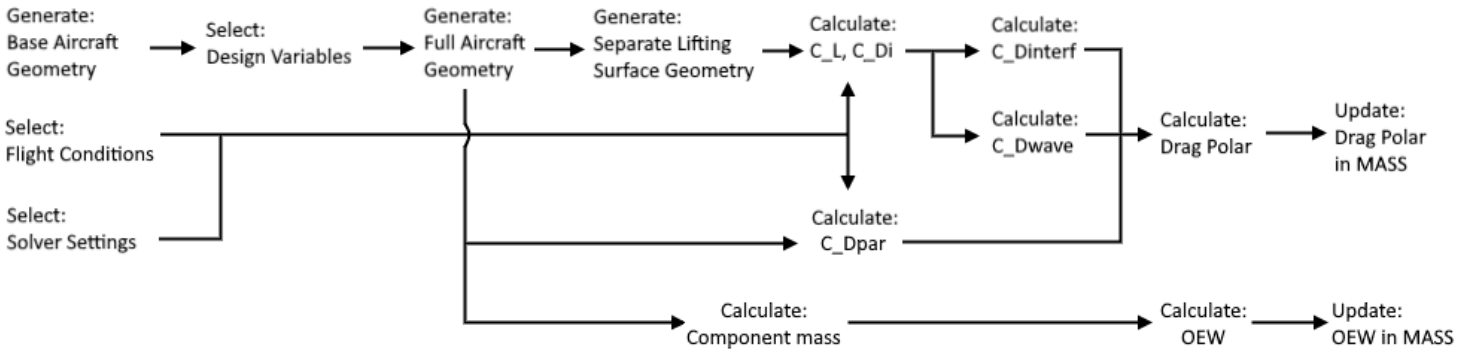

Figure 3.1: The workflow of the extension of MASS.

The aircraft are modeled in an open-source parametric aircraft modeling tool called 'OpenVSP'[1] (Open Vehicle Sketch Pad). The tool was initially developed by NASA [39], and was made available to the public domain in 2012. The tool is suitable for this project due to the following reasons:

- It allows for the creation and variation of any conceptual aircraft configuration based on its set of fully parameterized aircraft components;
- It has fast aerodynamic calculation capabilities;
- Every task in OpenVSP can be executed via command line, which allows for automated design and optimization processes.

The geometry generation is performed with OpenVSP, whereas the aerodynamic computations partially rely on that program. Matlab is used to automate processes that occur in OpenVSP. Referring to Figure 3.1, automation happens from 'Generate: Full Aircraft Geometry' onward.

[1] http://openvsp.org/, visited on 21 May 2020

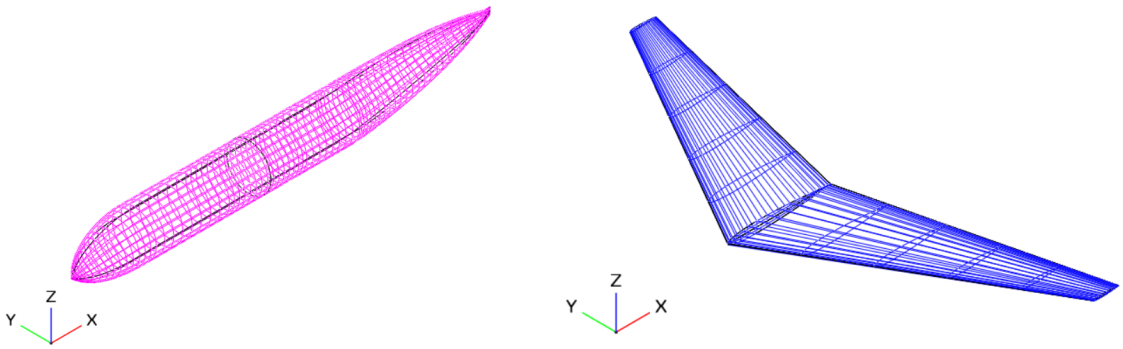

(a) The fuselage base geometry.

(b) The wing base geometry.

Figure 3.2: The base geometries used from OpenVSP.

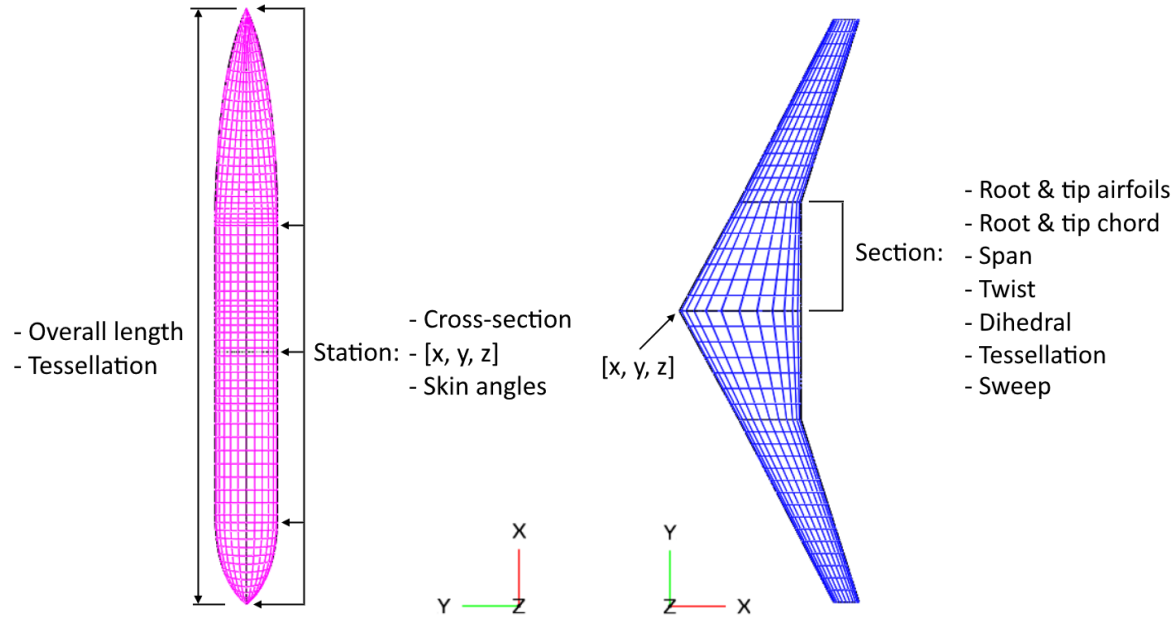

(a) The fuselage geometry parameterization.

(b) The wing geometry parameterization.

Figure 3.3: The parameterization of the base geometries used from OpenVSP.

3.1. Aircraft Geometry Modeling

The aircraft geometry is generated using OpenVSP. Via its graphical user interface (GUI), aircraft components are modeled using inbuilt base geometries representing the fuselage and wing. The geometries can be seen in Fig. 3.2a and 3.2b respectively. Those are 3D shapes whose surfaces are discretized into quadrilateral panels.

The fuselage base geometry is used to model all the non-lifting components. Those include the fuselage and the nacelles. The wing base geometry is used to model all lifting surfaces and wing-like structures. That encompasses structures such as the main wing, vertical and horizontal stabilizer, and pylons. Assigning the appropriate base geometry to a component is important since it influences its aerodynamics. The parameterization for each base geometry is summarized in Fig. 3.3a and 3.3b.

The aircraft described in Sections 3.1.1 to 3.1.2 form the set of the base models used for validation of the methodology.

3.1.1. A320 Geometry

The A320 is chosen since it is a widely used aircraft and representative for LPA. It comes with either the current engine option (ceo) or the new engine option (neo). Apart from the different engine, the A320neo also boasts sharklets on its main wing. The TLAR and other general parameters for both

aircraft variants can be found in Table 3.1.

Table 3.1: The TLAR and properties of the two A320 variants [12–16] and CSR-01[2].

Parameter	A320ceo	A320neo	CSR-01
MTOW [kg]	73500	79000	77000
OEW [kg]	41310	44300	42100
MZFW [kg]	61000	62800	62100
MLW [kg]	64500	66300	64500
$m_{PL,des}$ [kg]	14250	-	13608
$m_{PL,max}$ [kg]	20400	19250	20000
$m_{f,des}$ [kg]	17940	-	-
$m_{f,max}$ [kg]	24240	21005	18700
S [m^2]	122.4	122.4	122.41
b [m]	34.1	35.8	34.07
M_{cr} [-]	0.78	0.78	0.78
M_{MO} [-]	0.82	0.82	0.82
h_{cr} [m]	11278	11278	10668
R [nm]	2750	3400	2750
pax [-]	150	150	150
$s_{TO,SL}$ [m]	2180	1950	2200
$s_{L,SL}$ [m]	1440	-	1850
Engine (x2)	CFM 56-5A3	CFM LEAP-1A26	V2527-A5

The aircraft are modeled in OpenVSP as shown in Figures 3.4 and 3.5.

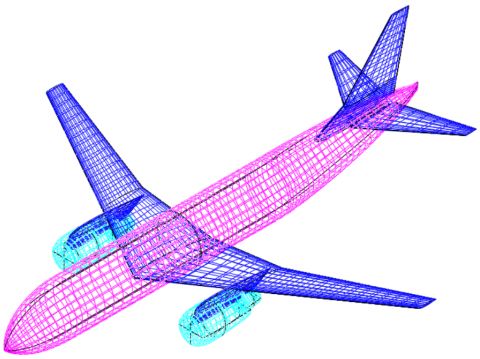

Figure 3.4: The A320ceo geometry in OpenVSP

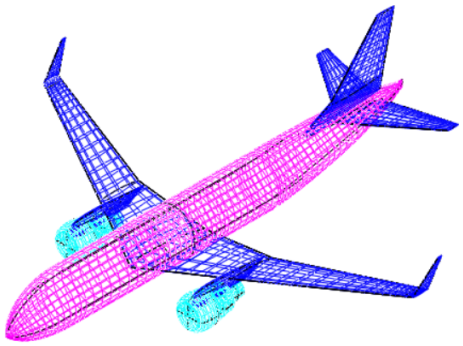

Figure 3.5: The A320neo geometry in OpenVSP

The geometries are modeled closely after technical drawings from Airbus [40] and the values indicated in Table 3.1. However, the airfoils are obtained differently. The main wing's airfoils are taken from the book written by Obert [17]. Furthermore, the horizontal stabilizer's airfoil is assumed to be zero-cambered and vary linearly from NACA 0012 to NACA 0009 from root to tip. The variation in thickness is done to match the model with the technical drawings. The vertical tail is modeled in similar fashion: From root to tip, NACA 0012 and NACA 0010 are used respectively. The result is a closed and meshed geometry for each A320 variant with color coded components.

3.1.2. CeRAS CSR-01 Geometry

The CeRAS CSR-01 is chosen due to its availability and similarity with the A320 regarding top level aircraft requirements (TLAR). Its key parameters are written in Table 3.1.

The aircraft is modeled in OpenVSP using the following references: the values from Table 3.1, an .stl model received from RWTH Aachen University, and the website[3]. The website in particular contains

[2] http://ceras.ilr.rwth-aachen.de/trac/wiki/CeRAS/AircraftDesigns/CSR01/KeyAircraftCharacteristics, visited on 21 May 2020.

[3] http://ceras.ilr.rwth-aachen.de/trac/wiki/CeRAS/AircraftDesigns/CSR01, visited on 21 May 2020

detailed information on main wing and airfoil geometries. The resulting geometry is depicted in Figure 3.6. Note that the geometry does not include any pylons and landing gear.

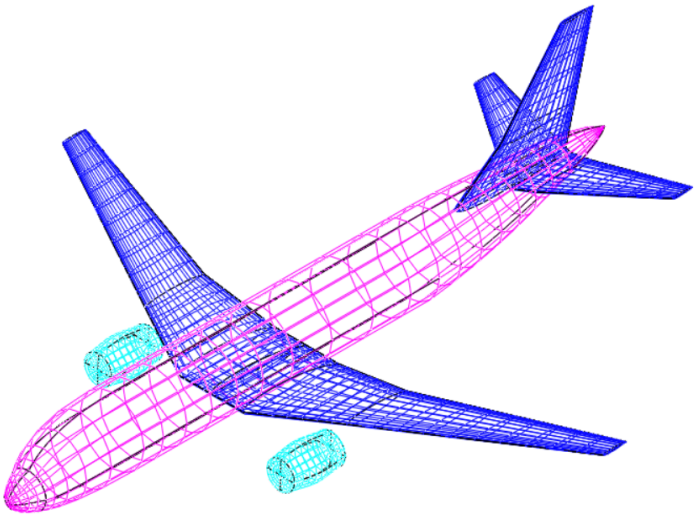

Figure 3.6: The CSR-01 geometry in OpenVSP.

3.2. Aerodynamics Module

Calculation of the aerodynamic coefficients for lift and drag is the aim of the aerodynamic extension of MASS. The methodology is inspired by Gur et al. [41] and constitutes of C_L, and C_D that is broken down into four components. Those components and their calculation methods are as shown below:

- C_{D_i}: VLM method employed by OpenVSP's aerodynamic module VSPAero. C_L is also calculated this way. See Section 3.2.1;
- $C_{D_{par}}$: Form factor method employed by OpenVSP. See Section 3.2.2;
- $C_{D_{interf}}$: Wing-body interference drag increment based on Hoerner [42]. See Section 3.2.3;
- $C_{D_{wave}}$: Summation of each wing strip's local wave drag. See Section 3.2.4.

3.2.1. Lift-Induced Drag, C_{D_i}, and Lift Coefficient, C_L

The calculation of C_L and C_{D_i} happens with the aerodynamic module VSPAero that is integrated within OpenVSP. The module employs a linear VLM method that uses the Trefftz-plane approach to calculate induced drag. It is a fast, linear method which is suitable for assessing aerodynamics at a conceptual level. Its accuracy is investigated in a comparison study conducted by Quitter et al. [8]. In that paper, VSPAero is compared against aerodynamic results from: wind tunnel testing, Star CCM+ (RANS CFD), and FlightStream (surface vorticity solver). A biplane-winglet configuration is studied among others, and the results for C_L and C_D are shown in Figure 3.7. The C_L prediction from VSPAero comes close to the wind tunnel data. It should be noted that it cannot predict stall due to its linear nature. The C_D calculation by VSPAero is reported to be underestimated. That can be improved by following the proposed drag build-up approach from this thesis.

In this project only the lifting surfaces of the aircraft, i.e. the main wing and horizontal stabilizer, are included for this module. This is because they are assumed to be the only contributions to lift and induced drag. The 3D geometries of these components are generated in OpenVSP and discretized into quadrilateral panels. As seen in Equations 3.1 up to 3.4 [43], the lift, side force and induced drag are calculated based on the circulation strength per wing strip. VSPAero outputs the coefficients corresponding to those forces.

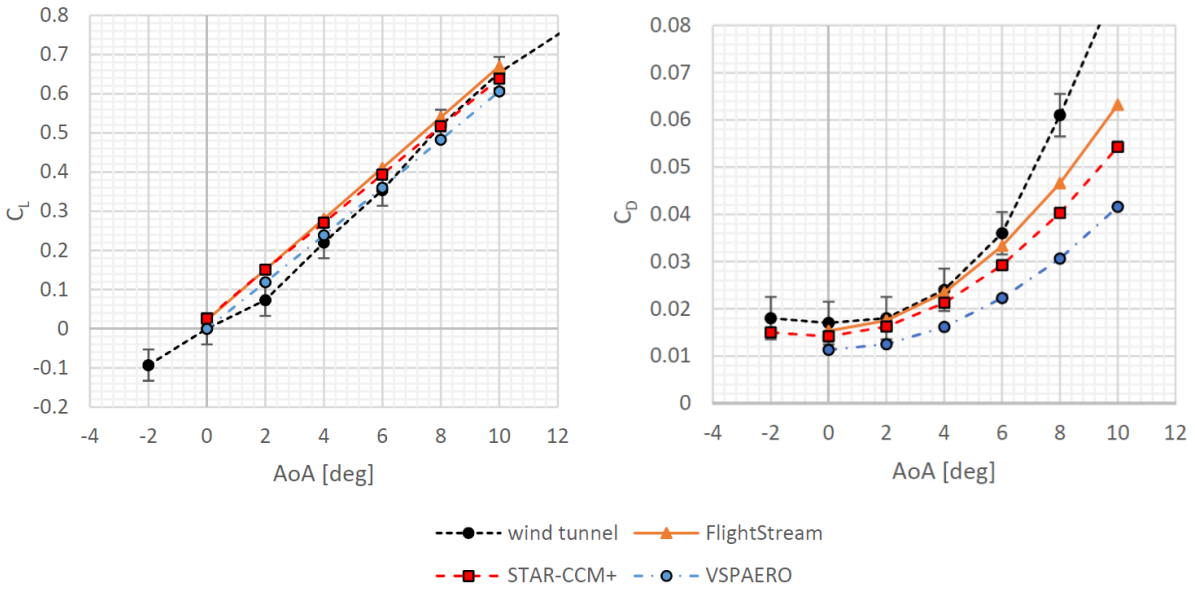

Figure 3.7: The comparison of C_L-α and C_D-α curves for a biplane-winglet configuration between aerodynamic solvers of varying fidelity. [8]

$$\Delta\phi_i = \sum_{strip} \bar{\Gamma}_i \tag{3.1}$$

$$L = \sum_{i=1}^{N} \Delta\phi_i \cos\theta_i \Delta s_i \tag{3.2}$$

$$Y = \sum_{i=1}^{N} -\Delta\phi_i \sin\theta_i \Delta s_i \tag{3.3}$$

$$D_i = -\frac{1}{2}\rho_\infty \sum_{i=1}^{N} \Delta\phi_i \frac{\partial\phi}{\partial n_i} \Delta s_i \tag{3.4}$$

For this module, all inputs and relevant outputs are captured in Table 3.2. The input β is not considered in this study since longitudinal flight is assumed. Moreover, the cg location does not affect the lift and induced drag.

Table 3.2: All inputs and relevant outputs from the lift-induced drag calculations.

Inputs	3D geometry of lifting surfaces, Mach, α, β, cg location
Outputs	C_L, C_{D_i}

3.2.2. Parasite Drag, $C_{D_{par}}$

Parasite drag calculation for the whole aircraft configuration is done using handbook methods. Essentially it is the summation of the parasite drag of individual aircraft components. For n total number of aircraft components, the parasite drag is calculated using Equation 3.5[4].

$$C_{D_{par}} = \frac{\sum_{k=1}^{n} S_{wet,k} Q_k C_{f,k} FF_k}{S_{ref}} \tag{3.5}$$

S_{ref} is the main wing planform area. The four terms behind the sigma are obtained as follows:

- S_{wet}: The 3D geometry of the full aircraft is to be modeled beforehand in OpenVSP. The program then computes the wetted surface area of each component and accounts for any overlap.

[4] http://openvsp.org/wiki/doku.php?id=parasitedrag, visited on 21 May 2020

- Q: Since the interference drag is calculated separately for the main wing-body junction (see Section 3.2.3), its interference term Q is set to 1. Other junctions have non-unity Q values as proposed by Raymer [44]: Horizontal stabilizer (Q = 1.08), vertical tail (Q = 1.03), and nacelle (Q = 1.3).
- C_f: The skin friction coefficient is determined based on the component's local percentage laminar flow and Reynolds number, Re_k. The percentage laminar flow is assumed to be 0, since it is not present in transonic cruise [44]. This means that all flows are fully turbulent. Re_k is then only dependent on the flight conditions and component reference length. Since the reference length is automatically derived from the geometry, only the flight conditions require manual input. The ambient conditions are derived from the US Standard Atmosphere model from 1976. The relation between Re_k and C_f for fully turbulent flow is given by Equation 3.6.

$$C_f = \frac{0.455}{\log Re_k^{2.58}} \tag{3.6}$$

- FF: The form factor equations for wings and bodies are given by Equations 3.7 and 3.8 respectively.

$$FF = 1 + 2\left(\frac{t}{c}\right) + 60\left(\frac{t}{c}\right)^4 \tag{3.7}$$

$$FF = 1 + \frac{1.5}{\left(\frac{l}{d}\right)^{1.5}} + \frac{7}{\left(\frac{l}{d}\right)^{3}} \tag{3.8}$$

The input and outputs of this module are summarized in Table 3.3.

Table 3.3: Inputs and outputs from the parasite drag calculations.

Inputs	3D geometry of the whole aircraft, Mach, altitude, Q, S_{ref}
Outputs	$C_{D_{par}}$

3.2.3. Interference Drag, $C_{D_{interf}}$

In section 3.2.2 the interference term Q is fixed for three major intersections: horizontal stabilizer, vertical tail, and nacelle. For the main wing-body intersection, Gur et al. [41] describe an alternative method to calculate the corresponding interference drag. For wings with t/c smaller than 0.075 at the root, Equation 3.9 [45] applies. It is a statistical relation derived from CFD computations.

$$\begin{aligned} C_{D_{interf}} \frac{S_{ref}}{c^2} = {} & 0.1112 - 0.2572 \sin\phi + 3.440(t/c) - 0.02097 \log_{10} Re_c + 0.09009 \sin^2\phi \\ & - 2.549(t/c)\sin\phi + 0.03010 \log_{10} Re_c \sin\phi - 0.1462(t/c)\log_{10} Re_c \end{aligned} \tag{3.9}$$

For other wing root thicknesses, Equation 3.10 from Hoerner [42] are used. The first part of the equation is due to joining the wing with the fuselage. The trailing part of the equation is due to the wing-body intersection angle. The total interference drag is obtained by adding these contributions together for each main wing-body junction present.

$$C_{D_{interf}} = \left(0.75\frac{t}{c} - 0.0003\left(\frac{t}{c}\right)^{-2}\right)\frac{t^2}{S_{ref}} + 0.015\left(-0.07 * d\alpha * b^2/S_{ref}\right)^2 \tag{3.10}$$

To obtain the wing characteristics at the wing-fuselage intersection, the parametric geometry model is exploited. Since the fuselage diameter is known, the corresponding wing strip can be located. Then, its cross-sectional properties can be derived, such as local chord and thickness.

3.2.4. Wave Drag, $C_{D_{wave}}$

The wave drag is assumed to be only present on the lifting surfaces. The paper by Gur et al. [41] suggests using wave drag increments for each wing strip, which are obtained by applying Equations 3.11 to 3.15.

$$M_{DD} = \frac{\kappa_A}{\cos \Lambda_{0.5}} - \frac{C_l}{10 \cos \Lambda_{0.5}{}^3} - \frac{t/c}{\cos \Lambda_{0.5}{}^2} \tag{3.11}$$

$$\kappa_A = \begin{cases} 0.95 & \text{for supercritical airfoils} \\ 0.87 & \text{for conventional airfoils} \end{cases} \tag{3.12}$$

$$M_{cr} = M_{DD} - \sqrt[3]{\frac{0.1}{80}} \tag{3.13}$$

$$C_{d_{wave}} = \begin{cases} 0 & M \leq M_{cr} \\ 20(M - M_{cr})^4 & M > M_{cr} \end{cases} \tag{3.14}$$

$$\Delta C_{D_{wave}} = C_{d_{wave}} \frac{S_{strip}}{S_{ref}} \tag{3.15}$$

There are some notes and assumptions concerning some of the equations. In addition to the wing geometry, Equation 3.11 uses the wing strip lift coefficient C_l derived from the VSPAero computations (see Section 3.2.1). This means that this module can only be used after the induced drag computations. Furthermore, two other equations have underlying assumptions. Equation 3.13 assumes a fixed offset between M_{cr} and M_{DD} for all airfoils. Equation 3.14 prescribes Lock's fourth power law for all airfoils when the freestream Mach number is higher than the local critical Mach number.

3.3. Aerodynamics Module Validation

This section covers the validation aspect of the aerodynamic module. First, effects of the surface mesh are treated in Section 3.3.1. The subsequent sections discuss the results produced using the reference aircraft models.

3.3.1. Wing Meshing

A study has been performed to assess the impact of mesh refinement on C_L, C_{D_i}, and $C_{D_{par}}$. A similar wing to the A320ceo's is used as baseline, which can be seen in Figures 3.8 to 3.11. The flight conditions are as follows: Mach = 0.78 and h = 11278 m. The number of panels is varied in longitudinal direction. In OpenVSP it is done by changing the tessellation value from 13 up to 113. The total number of panels in longitudinal direction equals the tessellation value minus one. That total number includes both upper and lower surfaces. There is an equal amount of panels on the upper as well as on the lower side. Hence tessellation always has an odd numbered value. The size of the panels become smaller towards the leading and trailing edges.

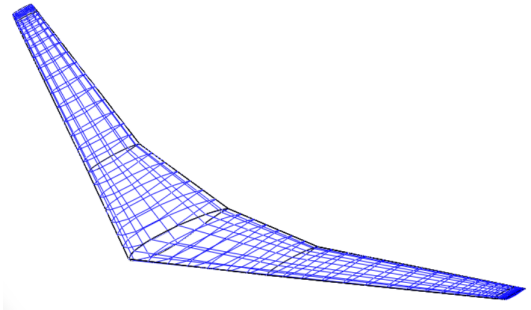

Figure 3.8: A wing with a longitudinal tessellation of 13.

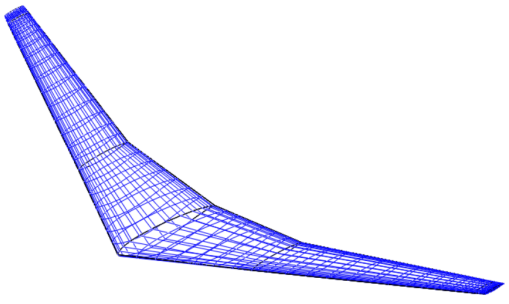

Figure 3.9: A wing with a longitudinal tessellation of 25.

The computations are done for -2 to 8 degrees α, leading to the graphs in Figure 3.12. All four curves overlap, meaning that the tessellation does not affect the C_L-C_{D_i} curve significantly.

Regarding the parasite drag, the results are tabulated in Table 3.4. The values of $C_{D_{par}}$ approach 0.00739 as the tessellation increases. At a tessellation of 25, $C_{D_{par}}$ already has an difference of below 0.2% from the values at higher tessellation. This means that 25 can be used reliably as tessellation value for the wing geometry in later analyses.

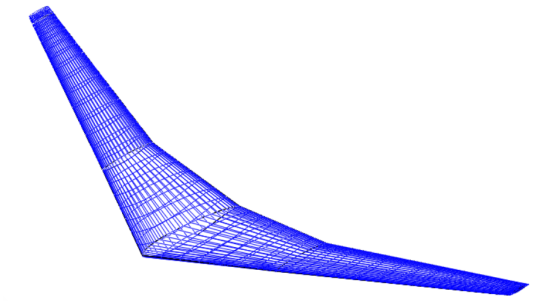

Figure 3.10: A wing with a longitudinal tessellation of 49.

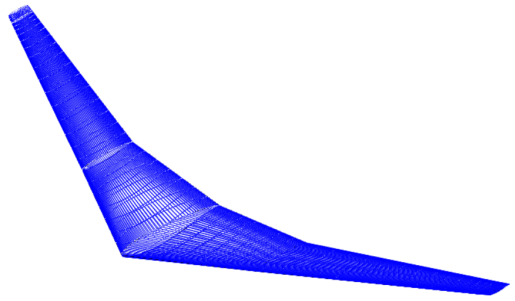

Figure 3.11: A wing with a longitudinal tessellation of 113.

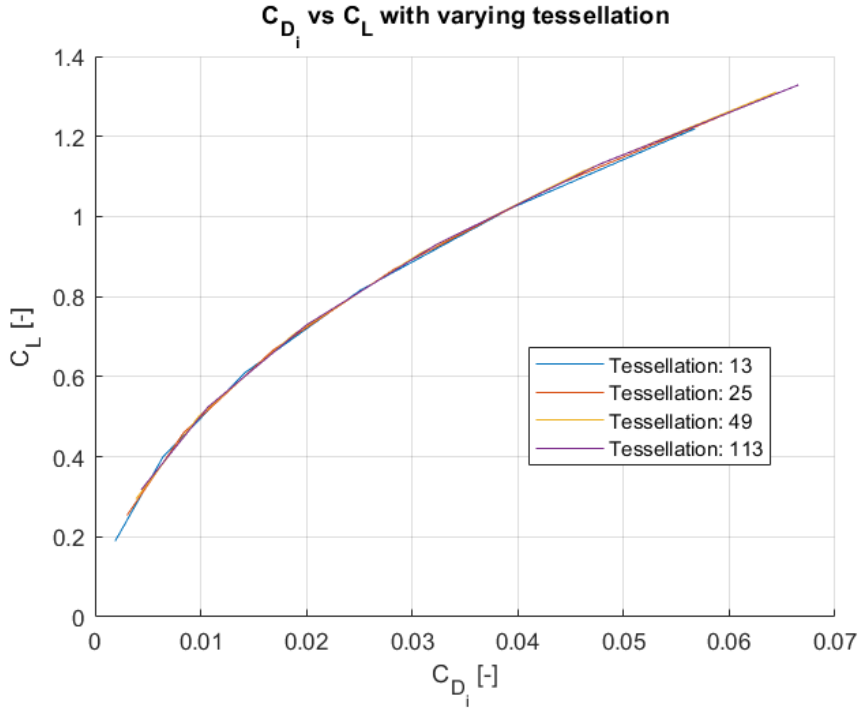

Figure 3.12: Induced drag and lift coefficients of a planar wing, with varying tessellation.

Table 3.4: Parasite drag of a planar wing for different levels of mesh refinement.

Tessellation	13	25	49	113
$\mathbf{C}_{D_{par}}$ [-]	0.00716	0.00738	0.00739	0.00739

3.3.2. Validation Using A320

The geometry of the A320ceo is modeled as seen in Figure 3.4. The computations have been performed using the reference values from Table 3.5. The resulting drag polars can be seen in Figure 3.13, along with two reference polars from Obert [17].

Table 3.5: Cruise flight conditions and reference values of the A320ceo.

Mach [-]	0.5, 0.78	$\mathbf{S}_{ref}$ [m^2]	122.4
h [m]	11278	$\mathbf{b}_{ref}$ [m]	34.1
α [deg]	[-4, 8]	$\mathbf{c}_{ref}$ [m]	4.29

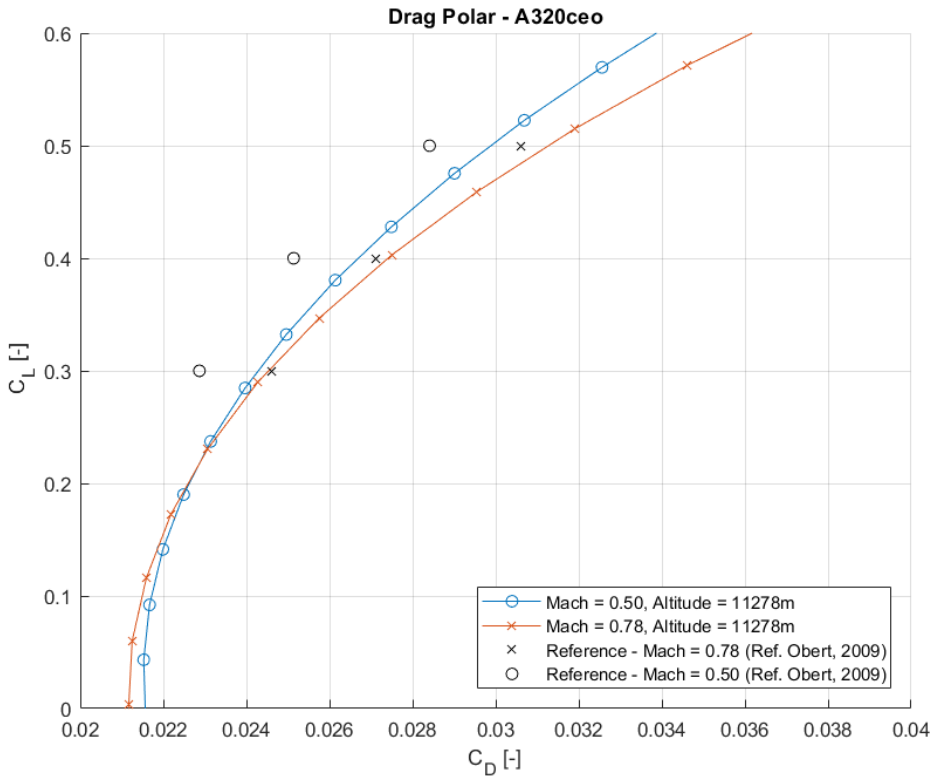

Figure 3.13: The A320ceo drag polars at cruise. Flight conditions correspond with values from Table 3.5.

In Figure 3.13, there is a good correspondence between the 0.78 Mach curves. At 0.5 Mach, there is a 5.3% maximum deviation with the reference data. This occurs at C_L = 0.3, which falls outside the cruise region of C_L = 0.5 to 0.6. Even though there is no perfect correspondence with the reference, the produced drag polars have sufficient accuracy for conceptual level studies with MASS.

3.3.3. Validation Using CSR-01

The CSR-01 geometry can be seen in Figure 3.6. Aerodynamic analysis has been performed using the values from Table 3.6, resulting in the drag polar in Figure 3.14. The reference drag polar is retrieved from the online documentation[5]. The reference polar is calculated by RWTH Aachen University using handbook methods.

Table 3.6: Cruise flight conditions and reference values of the CSR-01.

Mach [-]	0.5, 0.78	$\mathbf{S}_{ref}$ [m^2]	122.41
h [m]	10668	$\mathbf{b}_{ref}$ [m]	34.07
α [deg]	[-2, 8]	$\mathbf{c}_{ref}$ [m]	4.18

[5] http://ceras.ilr.rwth-aachen.de/trac/wiki/CeRAS/AircraftDesigns/CSR01/Aerodynamics, visited on 23 May 2020

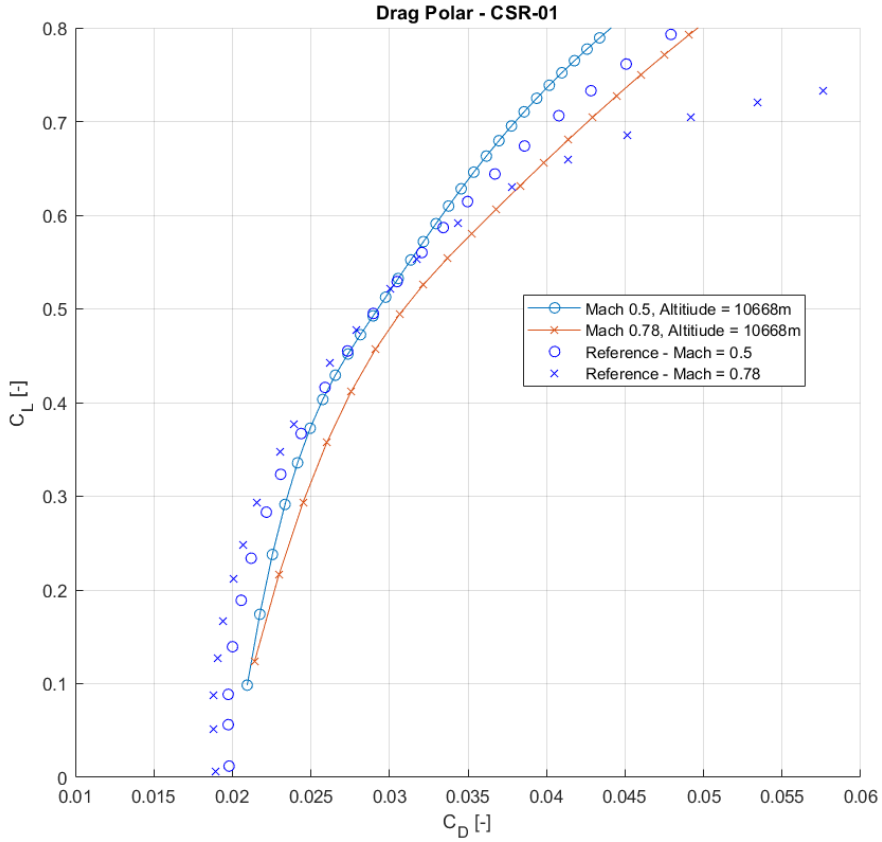

Figure 3.14: The CSR-01 drag polars. Flight conditions correspond with values from Table 3.6.

Although curves come close to their references between C_L = 0.2 and 0.6, there are some discrepancies. To see the differences in greater detail, the available reference drag breakdown at 0.78 Mach and C_L = 0.54 is captured in Table 3.7. Here, the viscous drag component is the summation of parasite and interference drag components.

Table 3.7: Drag breakdown of CSR-01 at Mach = 0.78 cruise.

	Current Method	**Reference**[6]	**Difference [%]**
$\mathbf{C}_L$ [-]	0.54	0.54	-
$\mathbf{C}_D$ [-]	0.03319	0.03092	7.34
$\mathbf{C}_{D_i}$[-]	0.01148	0.01106	3.80
$\mathbf{C}_{D_{viscous}}$ [-]	0.01820	0.01884	-3.40
$\mathbf{C}_{D_{wave}}$ [-]	0.00351	0.00102	244.5

The differences in induced and viscous drag are within 5% error and are accurate enough for use in MASS. However, the largest drag difference is found to be the wave drag. This overestimation is caused by M_{DD} and Equation 3.14. The sources of errors are listed below:

- M_{DD} is derived from κ_a which has the same value within the category of supercritical airfoils.
- M_{DD} values of 0.722 minimum are found on several strips of the main wing, while M_∞ = 0.78. Exceeding M_{DD} would never happen during normal operation;

[6] http://ceras.ilr.rwth-aachen.de/trac/wiki/CeRAS/AircraftDesigns/CSR01/Aerodynamics, visited on 23 May 2020.

- The fixed Mach offset assumption from Equation 3.13 is assumed to hold for all airfoils;
- The same type of curve is applied to all wave drag computations, see Equation 3.14.

Especially the second bullet is a sign that wave drag is overestimated. In this case, the wave drag prediction method underpredicts M_{DD} resulting from Equation 3.11. To overcome this, another method should be employed or κ_a be increased.

The error of the total C_D remains within 7.34%. The calculated drag polars display sufficient agreement with their respective references around cruise C_L.

3.3.4. Aircraft Trim

So far the drag polars shown represent the untrimmed condition of the aircraft. The influence of trimmed flight on the untrimmed drag polar is investigated in this section. The idea is to plot the untrimmed polar against the trimmed one and identify the differences. In the point-mass model of MASS only the three longitudinal degrees of freedom are taken into account: x, z, θ. The analysis will therefore only concern longitudinal trimmed flight. The aircraft model used is the A320neo, since it is also used in later analyses (see Chapter 4). The conditions for longitudinal trim are that the net forces and pitching moment about the center of gravity (cg) are zero. In the untrimmed condition, however, the net moment is non-zero. For the A320neo, that can be brought to zero by deflecting the all-moving stabilizer to a certain angle. This is done with the following assumptions:

1. The drag forces are very small compared to the lift forces, so their contributions to the pitching moment can be neglected [46];
2. Similarly, thrust contributions to the pitching moment are neglected since their moments are small compared to the moments caused by lift [46];
3. The cg is fixed at 28%-MAC based on Airbus' weight and balance document[7].

Since the stabilizer's deflection angles are unknown, a range from -3 to 3 degrees is used to obtain the drag polars. This resulted in the curves in Figure 3.15.

The first observation is that the slope of the curves is negative, indicating longitudinally stable behavior. Furthermore, the C_L values at trim correspond with $C_M = 0$, so the deflection angle at trimmed cruise flight can be derived. At $C_{L,cr} = 0.55$, the stabilizer is deflected downward at 0.66 deg with respect to the aircraft's centerline. In reality aircraft trim is also achieved with minimal deflection angles to limit trim drag. Since each C_L value has its own corresponding C_D, the trimmed drag polar can derived. Figure 3.16 shows the trimmed versus the untrimmed drag polar.

The difference at cruise C_L is 1 drag count, and remains similar in the surrounding regions. Therefore it can be assumed that the effect of longitudinal trim on the untrimmed drag polar is negligible. In the subsequent analyses the untrimmed drag polars will hence be considered as trimmed.

3.4. Weights Module

The total weight of the aircraft consists of three components: operational empty, payload, and fuel. The main concern of the framework extension is the estimation of operational empty weight (OEW). This is because airframe weight, which is part of OEW, is subjected to aircraft geometry variations.

The breakdown of the OEW components is as follows: [47–50]

- Airframe:
  - Wing;
  - Fuselage;
  - Horizontal stabilizer;
  - Vertical tail;
  - Landing gear;

[7] http://www.smartcockpit.com/docs/Getting_To_Grips_With_Weight_and_Balance.pdf, visited on 18 August 2020.

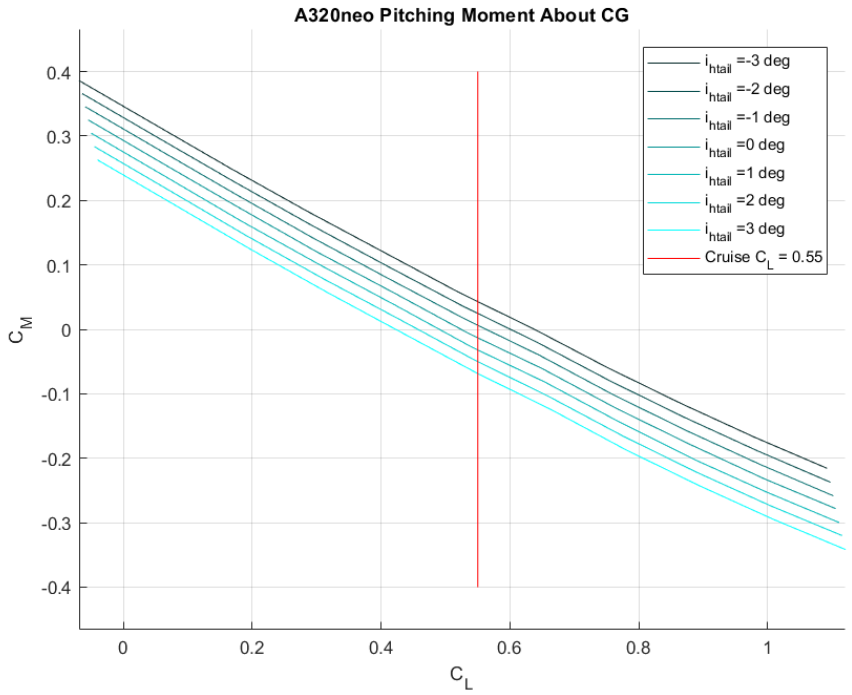

Figure 3.15: A320neo stabilizer deflection (i_{htail}) effects on the pitching moment about the cg.

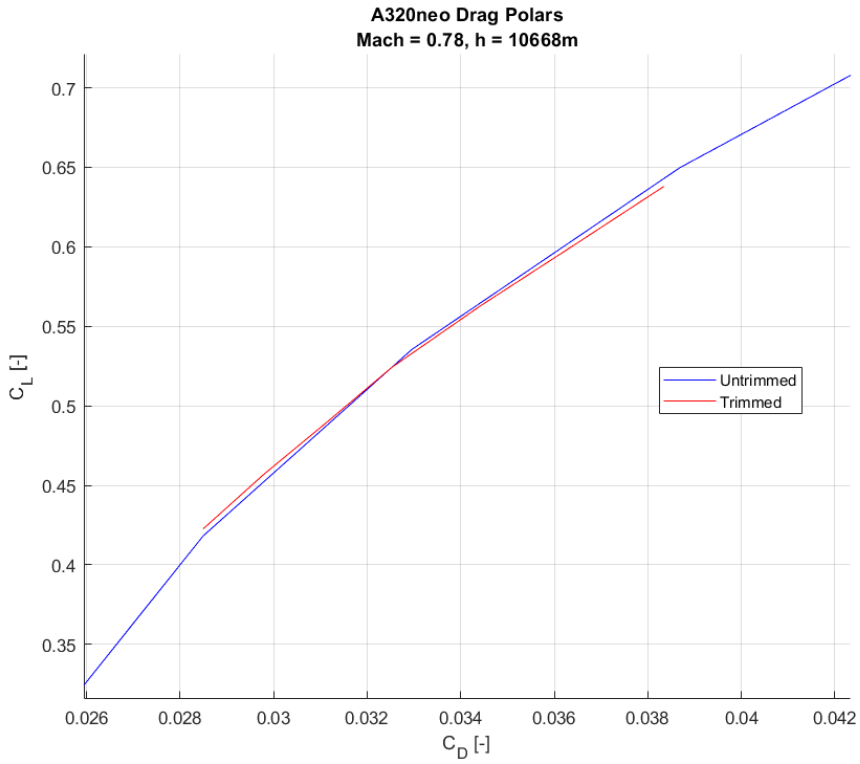

Figure 3.16: A320neo trimmed drag polar around cruise C_L = 0.55, plotted against the untrimmed drag polar.

- Propulsion:
  - Installed engines, nacelles, and pylons;
  - Engine control system, fuel system, oil system;
- Systems:
  - Auxiliary power unit (APU);
  - Instrumentation, navigational equipment, and electronics;
  - Hydraulic, pneumatic, and electrical systems;
  - Air-conditioning, anti-icing, and fire detection and prevention;
- Furnishings:
  - Flight deck accommodations;
  - Lavatory and toilet provisions;
  - Flooring and insulation;
  - Oxygen system;
  - Cargo restraints and handling equipment;
- Operational items:
  - Crew and passenger cabin supplies;
  - Potable water and toilet chemicals;
  - Residual fuel;
  - Safety equipment and escape provisions;
  - Pantry structure and provisions;
  - Passenger and flight attendant seats;

There are a number of methods to calculate each of the weight groups, referred to as Class-II weight estimation methods [18]. The methods in consideration should be able to capture aircraft geometry variations to be suitable for the aim of this study. The results vary judging from Tab. 3.8. Due to these differences, a combination of methods is used to obtain results of acceptable accuracy for point-mass performance. For example, for the wing weight, the method devised by Kundu [47] is chosen since it shows the smallest deviation with the reference and is of acceptable accuracy. The methods for other aircraft components are listed in Table 3.9.

Table 3.8: A320ceo main wing weight estimates from various Class II methods, compared with a reference datum from Obert [17].

Method	$\mathbf{m}_{wing}$ [kg]	**Difference**
Obert [17]	8801	0
Raymer [44]	5097	-42%
Kundu [47]	7488	-15%
Roskam (Torenbeek) [49]	6809	-22%
Roskam (General Dynamics) [49]	3923	-55%

Table 3.9: Weight equations for each aircraft component group.

	Component	**Method**	**Mass formula [kg]**
Airframe	Wing	Kundu [47]	$c_w k_{uc} k_{sl} k_{sp} k_{wl} k_{re} \left(MTOM \cdot n_{ult}\right)^{0.48} S_w^{0.78} A_w \left(1+\lambda\right)^{0.4} \times \left(1 - \frac{W_{f,w}}{MTOM}\right)^{0.4} / \left(\cos\left(\Lambda\right) \left(t/c\right)^{0.4}\right)$ (3.16)

	Fuselage	Kundu [47]	$c_{fus}k_e k_p k_{uc} k_{door}\left(2l_{fus}d_{fus}V_D^{0.5}\right)^{1.48}$	(3.17)
	Horizontal stabilizer	Raymer [44]	$0.4535923 * 0.0379K_{uht}\left(1+\frac{w_{fus,h}}{b_h}\right)^{-0.25} W_{dg}^{0.639} n_{ult}^{0.1} \times S_h^{0.75} l_{tail}^{-1} K_y^{0.704} \cos\Lambda_h{}^{-1} A_h^{0.166}\left(1+\frac{S_e}{S_h}\right)^{0.1}$	(3.18)
	Vertical tail	Kundu [47]	$0.0215\left(W_{dg}n_{ult}\right)^{0.48} S_v^{0.78} A_v\left(1+\frac{c_{v,tip}}{c_{v,root}}\right)^{0.4} / \left(\cos\Lambda_v\,(t/c)^{0.4}\right)$	(3.19)
	Main landing gear	Torenbeek [48]	$k_{uc}\left(18.1+0.131W_{dg}^{0.75}+0.019W_{dg}+2.23\cdot10^{-5}W_{dg}^{1.5}\right)$	(3.20)
	Nose landing gear	Torenbeek [48]	$k_{uc}\left(9.1+0.082W_{dg}^{0.75}+2.97\cdot10^{-6}W_{dg}^{1.5}\right)$	(3.21)
Propulsion	Nacelle	Kundu [47]	$6.7T_{en}n_{en}$	(3.22)
	Power plant	Kundu [47]	$1.4W_{en}n_{en}$	(3.23)
Systems	APU	Torenbeek [48]	$11.7\left(0.4V_{pass,cabin}\right)^{3/5}$	(3.24)
	Instruments, navigation, electronics	Torenbeek [48]	$0.347W_{de}^{5/9}R_D^{1/4}$	(3.25)
	Hydraulics	Torenbeek [48]	$0.011W_{de}+181$	(3.26)
	Electrical system	Torenbeek [48]	$0.02W_{dg}+181$	(3.27)
	Air-conditioning, anti-icing	Torenbeek [48]	$14\left(l_{pass,cabin}\right)^{1.28}$	(3.28)
	Anti-fire	Torenbeek [48]	$0.0012W_{dg}$	(3.29)
Furnishings	Flight deck accommodations	Torenbeek [48]	$9.1W_{de}^{0.285}$	(3.30)

	Lavatory provisions	Torenbeek [48]	$136n_{lav}$	(3.31)
	Floor covering	Torenbeek [48]	$1.25\left(S_{floor}^{1.15}\right)$	(3.32)
	Sound proofing	Torenbeek [48]	$6.17\left(V_{pass}+V_{cargo}\right)^{1.07}$	(3.33)
	Cargo restraints	Torenbeek [48]	$1.28V_{cargo}$	(3.34)
	Fixed oxygen system	Torenbeek [48]	$13.6+0.544n_{pax}$	(3.35)
	Cargo handling equipment	Torenbeek [48]	$\rho_{container}V_{cargo}$	(3.36)
Operator	Crew provisions	Torenbeek [48]	$93n_{flightcrew}+68n_{cabincrew}$	(3.37)
	Passenger cabin supplies	Torenbeek [48]	$8.62n_{pax}$	(3.38)
	Potable water, toilet chemicals	Torenbeek [48]	$1.36n_{pax}$	(3.39)
	Safety equipment	Torenbeek [48]	$0.907n_{pax}$	(3.40)
	Residual oil and water	Torenbeek [48]	$0.151V_{fueltank}^{2/3}$	(3.41)
	Passenger seats	Torenbeek [48]	$29.9\cdot\frac{n_{pax}}{3}+8.3n_{cabincrew}$	(3.42)
	Pantry structure	Torenbeek [48]	$113.4n_{maindish}+45.3n_{snack}$	(3.43)
	Escape provisions	Torenbeek [48]	$0.453n_{pax}$	(3.44)

3.5. Weights Module Validation

Table 3.8 showed that Class II weight estimation methods can predict inconsistent results. The weight estimation implementation therefore consists of a mix of methods to obtain results of acceptable accu-

racy. The aimed maximum deviation of predicted OEW is 10%. The weight components are calculated for the A320ceo and CSR-01, and put in Tables 3.10 and 3.11 respectively. The OEW for both aircraft remains below 1% with respect to their references.

Table 3.10: A320ceo weight breakdown comparison.

Component	**Method**	$\mathbf{m}_{computed}$ [kg]	$\mathbf{m}_{ref}$ [kg] [17]	**Difference [%]**
Wing	Kundu	7488	8801	-15.0
Fuselage	Kundu	8878	8938	-0.67
Horizontal stabilizer	Raymer	681	625	8.96
Vertical tail	Kundu	471	463	1.7
Landing gear	Torenbeek	2878	2275	26.5
Propulsion	Kundu	7964	8105	-1.74
Systems	Torenbeek	4900	4788	2.35
Furnishings	Torenbeek	3382	2813	20.2
Operational items	Torenbeek	3143	3215	-2.24
OEW	Summation	39785	40023	-0.59

Table 3.11: CSR-01 weight breakdown comparison.

Component	**Method**	$\mathbf{m}_{computed}$ [kg]	$\mathbf{m}_{ref}$ [kg][8]	**Difference [%]**
Wing	Kundu	7573	8097	-6.47
Fuselage	Kundu	9168	8986	2.03
Horizontal stabilizer	Raymer	724	682	6.16
Vertical tail	Kundu	571	522	9.39
Landing gear	Torenbeek	3014	2491	21.0
Propulsion	Kundu	8190	8990	-8.90
Systems	Torenbeek	5009	5378	-6.86
Furnishings	Torenbeek	3391	3006	12.8
Operational items	Torenbeek	4169	3939	5.84
OEW	Summation	41809	42092	-0.67

[8] http://ceras.ilr.rwth-aachen.de/trac/wiki/CeRAS/AircraftDesigns/CSR01/Mass%20Breakdown, visited on 23 June 2020.

4

Application

Before the extension of MASS, the framework had been used for parallel HEP parameter variation studies. With the extension of MASS, the effects of varying geometry can be incorporated as well. This chapter provides details on the effects on fuel burn by variations in powertrain (HEP) and geometry, and elaborates on the process involved.

The variations in geometry comes in two forms. The first is the change in planform geometry. The second is the change in airframe configuration. In Section 4.1 a commonly used conventional tube-and-wing (TAW) aircraft, the A320neo, is presented. Section 4.2 describes a blended wing-body which represents the configuration change of the A320neo. Section 4.3 at the end of this chapter summarizes the findings.

4.1. A320neo

The A320neo geometry is modeled in MASS using dimensions and technical drawings in the airport and maintenance planning document from Airbus [40]. The modeling approach is the same as for the A320ceo, which is described in Section 3.1.1. As opposed to the A320ceo, the A320neo has winglets as seen in Figure 4.1. Furthermore, as the A320neo uses a different engine, the nacelle and pylon dimensions differ as well.

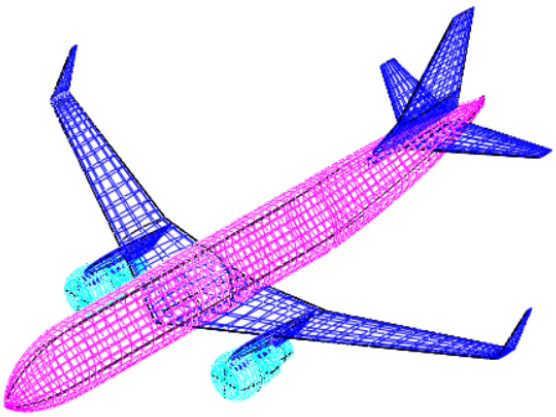

Figure 4.1: The modeled A320neo geometry.

Table 4.1: Mission parameters used in the parameter variation and optimization studies.

Variable	Value
M_{cr} [-]	0.78
h_{cr} [kft]	35
pax	150
R [nm]	800

Two parameter variation studies are performed with this A320neo model. The first is purely focused on the optimization of the powertrain variables, see Section 4.1.1. The second adds the planform variables to the design space, see Section 4.1.2. Throughout the variations, the same short-range mission is used in the simulations. The characteristics thereof are presented in Table 4.1. The mission consists of the following six flight phases: Taxi, take-off, climb, cruise, descent, and landing.

4.1.1. A320neo Powertrain Variations

The variations of the hybrid-electric powertrain of the A320neo is performed in three steps:

1. Select design variables;
2. Perform design of experiments;
3. Perform optimization for minimal fuel burn;

An assumption made in this study is the use of year 2035 technology, see Table 4.2. With current year (2020) technology HEP would be infeasible due to the low specific power and energy density of batteries. The use of a parallel HEP architecture enables the engine to be supported with electrical power from the batteries. This allows its core to be downsized due to the lowered shaft power requirements. The engine bypass ratio can then be increased and the engine core mass be decreased, leading to an improved fuel economy. The engine core scaling parameter s_{en} is therefore selected as a design variable. The engine is to be supported during high thrust-demanding flight phases such as take-off and climb. The share of power provided by the batteries during each of those phases is represented by the power split ϕ. The design space is hence covered by three design variables: s_{en}, ϕ_{TO}, and ϕ_{Cl}.

Table 4.2: The assumed technology for 2035. [6]

e_{bat} [Wh/kg]	η_{bat} [-]	p_{EM} [kW/kg]	η_{EM} [-]
500	0.925	7.5	0.95

Prior to the optimization, a design of experiments is conducted to observe the response of the objective function to variations in each of the design variables. The objective function in this case is the change in fuel burn of a HEP A320neo with respect to the non-HEP A320neo. The design space is sampled at the values of the design variables described in Table 4.3. The resulting contour plots of the fuel burn change are depicted in Figure 4.2, which are sorted based on s_{en}.

Table 4.3: The bounds and step sizes of the design variables used for the design of experiments of the HEP A320neo.

	ϕ_{TO} [-]	ϕ_{Cl} [-]	s_{en} [%]
Lower bound	0	0	85
Upper bound	0.2	0.2	100
Step size	0.02	0.02	5

Judging from the four subfigures from Figure 4.2, likely there is a stationary point around ϕ_{TO} = 0.04 and ϕ_{Cl} = 0.08. In fact, the contours seem to be centered around that point. The corresponding minimum fuel burn change is around -3.1% as observed in Figure 4.2b for s_{en} = 90%. The plots for s_{en} = 85% and 95% both show higher values for fuel burn change. This suggests that the local minimum found around s_{en} = 90% could be a global optimum.

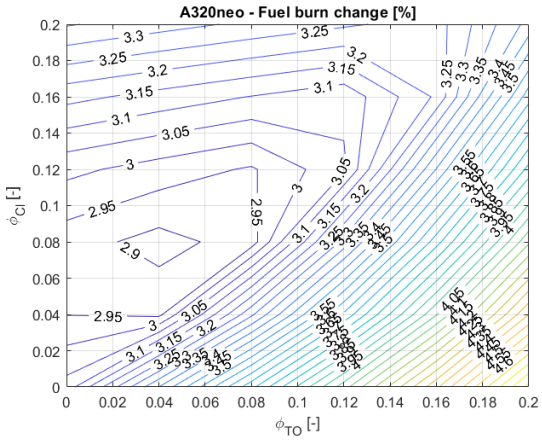

(a) s_{en} = 85%

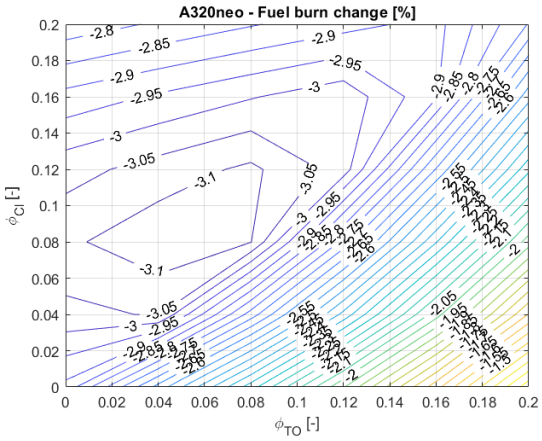

(b) s_{en} = 90%

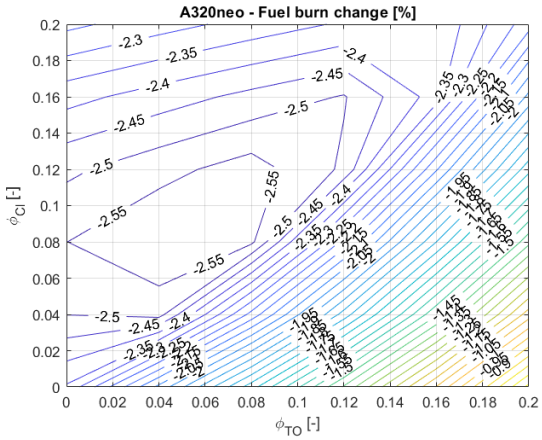

(c) s_{en} = 95%

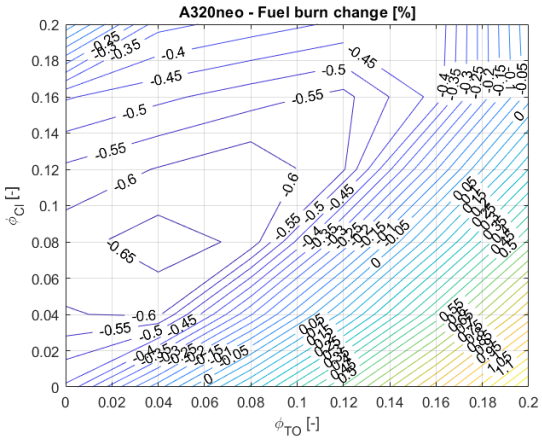

(d) s_{en} = 100%

Figure 4.2: The contour plots of the fuel burn change of the HEP A320neo with respect to the non-HEP variant.

The optimization problem is formulated based on the observations from the design of experiments, which can be seen below:

$$\begin{aligned} \min_{x} \quad & f(x) = m_{f,burn}(x)/m_{f,burn,0} - 1 \\ \text{subject to} \quad & 0 < \phi_{TO} < 0.1 \\ & 0 < \phi_{Cl} < 0.2 \\ & 87.5\% < s_{en} < 95\% \end{aligned}$$

The optimization problem is solved using an optimizer in Matlab called 'fmincon'. The starting point lies at the non-HEP A320neo, so ϕ = 0 and s_{en} = 100%. The result from the optimization is recorded in Table 4.4.

Table 4.4: The result from the A320neo HEP optimization.

	ϕ_{TO} [-]	ϕ_{Cl} [-]	s_{en} [%]	f [%]
x_0	0	0	100	0
x_{opt}	0.035	0.070	91.6	-3.1

The found optimum point lies within the bounds of the design space, and is close to the expected optimum point.

4.1.2. A320neo Powertain and Geometry Variations

The powertrain and geometry variation study is initially done using the same steps as for the powertrain variation study described in Section 4.1.1. During the analyses several complications are encountered, which have led to changes to the plan of attack. A chronological overview of the whole process is presented below:

1. Select design variables;
2. Conduct design of experiments;
3. Apply model corrections;
4. Reduce the dimensionality of the problem;
5. Perform design of experiments for surrogate modeling;
6. Implement a suitable surrogate model;
7. Perform surrogate optimization for minimal fuel burn.

The powertrain variation part in this study concerns the same design variables used for the previous study from Section 4.1.1. The geometry variation part involves the redesign of the planform. The wing is defined by many parameters as can be seen in Figure 3.3b. Since this is a study from a conceptual level perspective, certain parameters are left as constants. The airfoils for example remain constant since the analysis of changes in airfoil require a higher fidelity aerodynamic solver. Furthermore, the wing dihedral is left untouched since it affects lateral stability which is outside the research scope. Several other parameters remain unchanged based on their aerodynamic contribution and how much they are allowed to deviate. The parameters are analyzed one-by-one by plotting the drag polar for each change. For example in Figure 4.3, the change in tip chord length of the winglet, $c_{winglet}$, is limited as well as the corresponding aerodynamic effect.

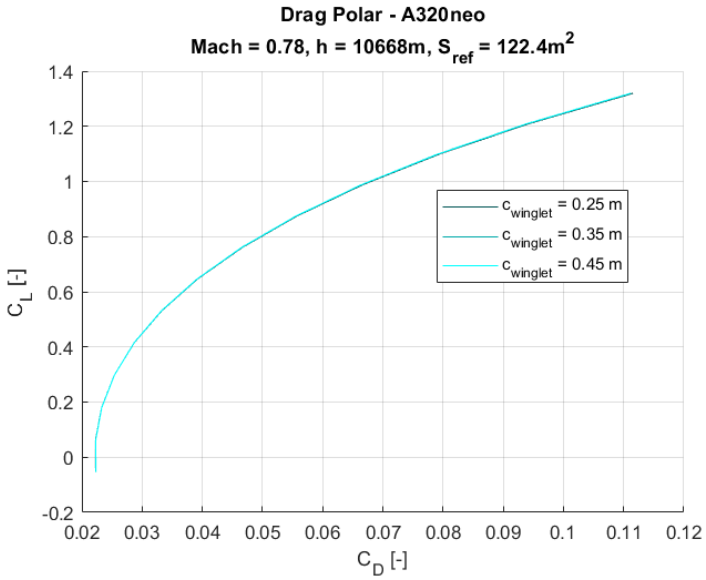

Figure 4.3: The drag polars of the A320neo corresponding to changes to $c_{winglet}$

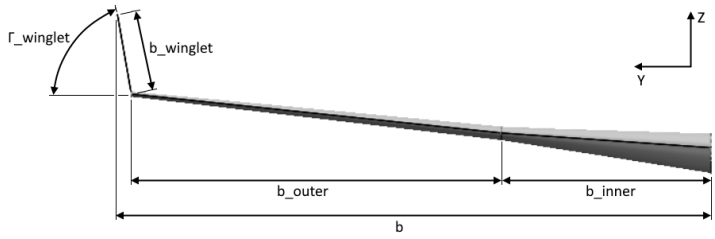

(a) The front view of the A320neo planform.

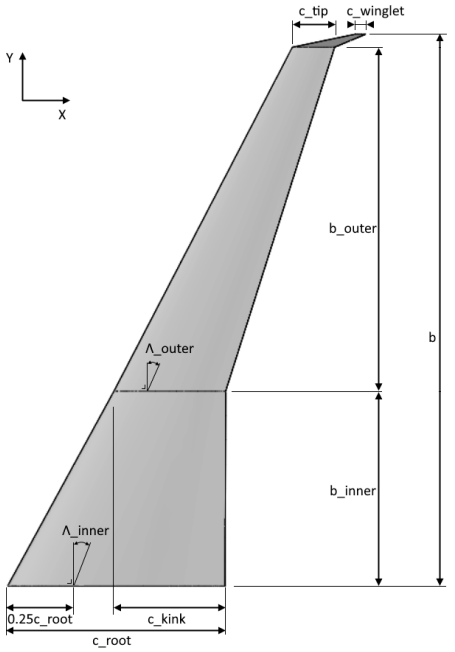

(b) The top view of the A320neo planform.

Figure 4.4: The chosen design variables of the A320neo.

The nine planform variables that are used in this study are listed as follows: c_r, b_i, Λ_i, c_k, b_o, Λ_o, Γ_w, c_t, and b_w. Figures 4.4a and 4.4b provide the explanation of the variables. Moreover, Table 4.5 provides corresponding the reference values.

Table 4.5: The reference values of the A320neo.

ϕ_{TO} [-]	ϕ_{Cl} [-]	s_{en} [%]	c_r [m]	b_i [m]	Λ_i [deg]	c_k [m]	b_o [m]	Λ_o [deg]	Γ_{wl} [deg]	c_t [m]	b_{wl} [m]
0	0	100	7.1	6.35	22.24	3.63	11.25	25	74	1.375	2.43

With the design variables known, a sensitivity analysis is performed for each about the reference values. It is found that for variations in inner and outer span, the wing weight deviates too much. For instance, Figure 4.5 shows the influence of b_{outer} on m_{OE}. The original trend shows that m_{OE} reduces by 1 ton for every -2m of total wing span, which suggests that a minimum wing area design would be best for fuel economy. A correction is therefore applied to curb the influence of planform parameters on mass. By taking the mass of the reference planform of the A320neo and dividing it by the surface area, the mass per unit area is obtained. This is then used to reflect the changes in mass due to planform variations. The results from the modified model are also plotted in Figure 4.5.

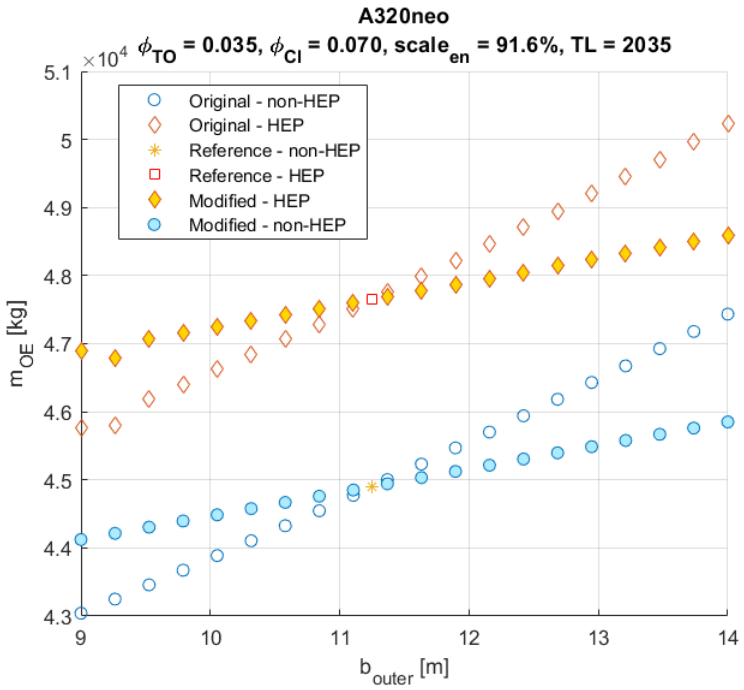

Figure 4.5: Effects on m_{OE} caused by variations in b_{outer} before and after modification of the weight model.

The new wing mass per unit surface area is shown in Table 4.6 along with other reference aircraft's for comparison. The wing masses of the reference aircraft are derived using Equation 4.1 [18]. The results from Table 4.6 are depicted in Figure 4.6 to show that the corrected value is sensible, as it aligns with the trend of the reference points.

$$m_{wing} = 68.22 \times 10^{-4} MTOW^{1.25} \tag{4.1}$$

Table 4.6: Comparison of wing weight per unit area. [18]

Aircraft	MTOW [kg]	m_{wing} [kg]	S_{ref} [m^2]	m_{wing}/S_{ref} $[kgm^{-2}]$
Fokker 50	20820	1706	70	24.4
Fokker 100	43090	4235	94	45.3
Boeing 737-200	52390	5407	91	59.3
Current (A320neo)	68452	8731	129	67.6
Boeing 727-300	95028	11382	153	74.4
Airbus A300-600R	170500	23636	260	90.9
Airbus A330-300	217000	31951	362	88.4
Boeing 777-200	242670	36744	427	86.1

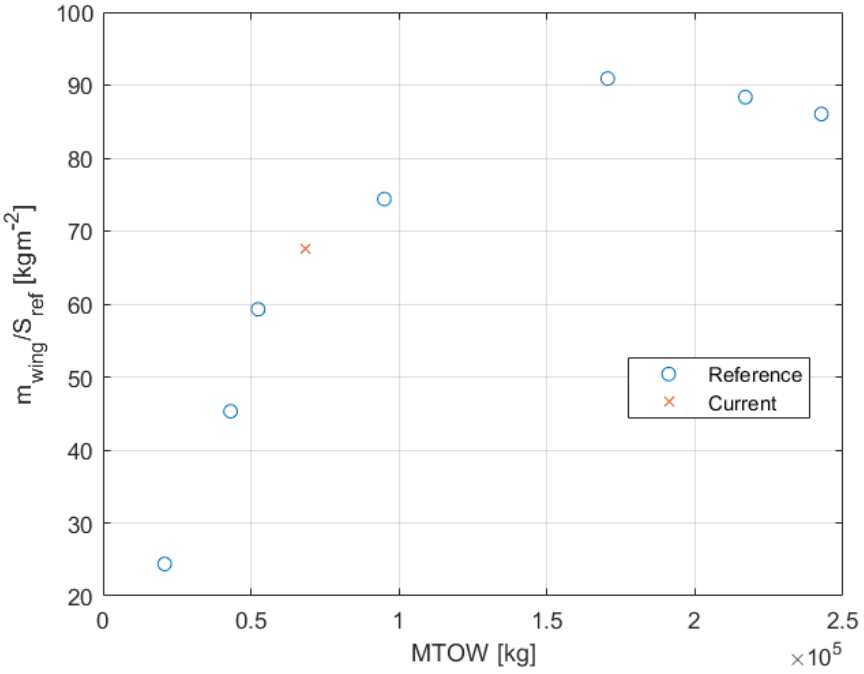

Figure 4.6: The wing weight per unit area based on values from Table 4.6.

After the modification, the aerodynamics are more influential on the fuel burn change than the mass. This is evident from Figure 4.7 where longer wing spans result in lower fuel burn. The wing bending moment about the longitudinal axis X is introduced as additional objective function to limit the wing span. Since the wing lift distributions and flight conditions are known, the bending moment can be calculated for any of the planform designs.

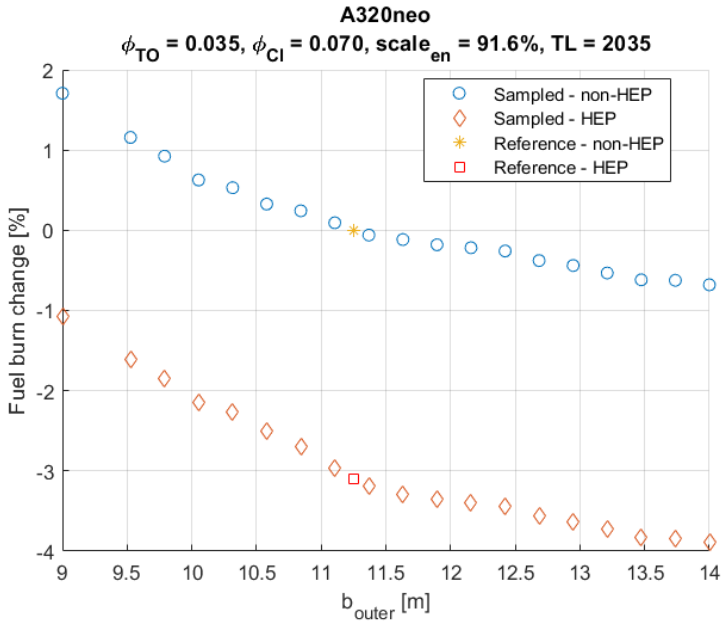

Figure 4.7: A320neo fuel burn change due to changes in b_{outer}.

Referring back to Figure 4.5, in the same plot there is a point that slightly deviates from the trend. It can be seen at about b_{outer} = 9.25m, on the modified and original HEP trend. This is caused during the aerodynamic computations by VSPAero. At times the solver would not fully converge or even stop

writing outputs during the task. These anomalies occur roughly 10% of the time. Data points that are not convergent can be recognized by constant fluctuations in C_L or C_{D_i} of the same magnitude as the values of the variables. Another way of recognizing erroneous data points are their corresponding incomplete output files. So there is an unreliability present which renders the use of automated optimizers on the model unsuitable. Hence a surrogate model is used to bypass this problem.

In order to obtain a surrogate model, a data set is required. Data can be more difficult to fit accurately the more variables and dependencies there are present. To reduce the time spent on obtaining the data and ease the fitting process, the number of design variables is lowered. This is done using the Matlab function 'corrcoef', which is short for correlation coefficient. It takes as input the observations of the design variables and corresponding objective functions. It then outputs two measures: The correlation coefficient R and p-value. The values of R range between -1 and 1, and indicate the level of dependence between the design variable and the objective value. Values of ± 1 indicate a strong dependence, whereas 0 expresses a weak dependence. The p-value tells whether or not to reject the null hypothesis that no relationship between the design variable and objective function is present. P-values below 0.05 indicate that there is a relationship. This means that the design variables that do not meet that requirement are left out of the optimization. The input data of 120 points is obtained using latin hypercube sampling (LHS) of the design space, bounded by the values written in Table 4.7. LHS can be compared to a rule of a sudoku-puzzle, where a number is only allowed to appear once in each row and column.

Table 4.7: The bounds used for the design variables in obtaining a data set with LHS.

	ϕ_{TO} [-]	ϕ_{Cl} [-]	s_{en} [%]	c_r [m]	b_i [m]	Λ_i [deg]	c_k [m]	b_o [m]	Λ_o [deg]	Γ_{wl} [deg]	c_t [m]	b_{wl} [m]
Lower bound	0	0	86.6	4.1	3.4	12.2	2.1	6.3	15	54	0.9	0.9
Upper bound	0.3	0.3	96.6	10.1	9.4	32.2	5.1	16.3	35	74	2.9	3.9

The function 'corrcoef' is used on the data, which results in the values seen in Tables 4.8 and 4.9. There are 5 variables selected based on their p-values: ϕ_{TO}, b_i, Λ_i, b_o, and c_t. The variable ϕ_{TO} is included to have a representation for HEP.

Table 4.8: The correlation coefficients and p-values for the design variables and fuel burn.

	ϕ_{TO}	ϕ_{Cl}	s_{en}	c_r	b_i	Λ_i	c_k	b_o	Λ_o	Γ_{wl}	c_t	b_{wl}	$m_{f,burn}/m_{f,burn,0}$
R	0.17	0.02	-0.03	0.02	0.25	-0.64	-0.01	-0.53	-0.05	0.05	0.17	-0.11	1
p	0.07	0.83	0.79	0.86	0.01	0	0.95	0	0.59	0.63	0.08	0.27	1

Table 4.9: The correlation coefficients and p-values for the design variables and wing bending moment.

	ϕ_{TO}	ϕ_{Cl}	s_{en}	c_r	b_i	Λ_i	c_k	b_o	Λ_o	Γ_{wl}	c_t	b_{wl}	$M_{x,wing}/M_{x,wing,0}$
R	0	0.13	-0.04	0.1	0.54	0.17	0.13	0.84	-0.08	-0.14	0.2	-0.14	1
p	0.96	0.18	0.67	0.29	0	0.08	0.18	0	0.43	0.15	0.04	0.14	1

With the reduction of the number of design variables from 12 to 5, an additional design of experiments is performed. Using LHS, 164 samples are obtained and fitted. Two different methods are used for fitting. One is a function in Matlab called 'stepwisefit' and the other is radial basis function (RBF) interpolation.

The function 'stepwisefit' essentially tries to fit a linear regression model by adding or removing a design variable one at a time. The data set is processed by the function, which returns a (linear) formula predicting the fuel burn change of a HEP A320neo with respect to its non-HEP variant. The formula is described in Equation 4.2.

$$m_{f,burn}/m_{f,burn,0} = 0 + 0.215\phi_{TO} + 0.241b_i - 0.614\Lambda_i - 0.489b_o + 0.194c_t \tag{4.2}$$

The formula is checked with the values found for the powertrain optimum, see Table 4.4. The predicted outcome is a -17.3% fuel burn change which does not correspond with the actual value of -3.1%. This method is therefore not used any further.

The RBF interpolation method fits the data using a weighted sum of the Gaussian function described by Equation 4.3[1].

$$f(r) = e^{-0.5r^2/\alpha^2} \tag{4.3}$$

Before fitting the data, 5 points are set aside to serve as test data. The fit set is consequently left with 159 points. Then the best RBF fit of the data is obtained by finding the right α value. A one dimensional optimization is performed using Matlab function 'fminbnd' with α as design variable. The objective function is the maximum deviation between the predicted and actual fuel burn change of the fit set, which is to be minimized. The found value for α is 5.44, and the predicted and actual fuel burn values of the test set are put in Table 4.10.

Table 4.10: The comparison between RBF prediction and actual fuel burn change.

Test point	RBF predicted fuel burn change [%]	Actual fuel burn change [%]
1	2.2	4.0
2	-6.9	-5.0
3	-8.1	-5.6
4	-2.6	-2.0
5	-3.7	-4.0

The largest deviation of 2.5% is observed at test point 3. Since the fuel burn change of the A320neo with optimized powertrain lies at -3.1%, the RBF fit is not accurate enough. Moreover, the fit both overpredicts and underpredicts, which renders it unreliable. This fit is therefore not used as well.

Two methods have not successfully fitted the data, so it is decided to use a different method which is based on artificial neural networks (ANN). An ANN is essentially a system of interconnected neurons or nodes that can be used to recognize patterns in data and form a prediction model [9]. The system consists of three types of layers in which the nodes reside: input, hidden, and output. Figure 4.8 shows the layers and the connections between the nodes. The information is feedforwarded from the input to the output layer through the links. Every link has its own strength or weight, which is determined with a specified algorithm when training the network.

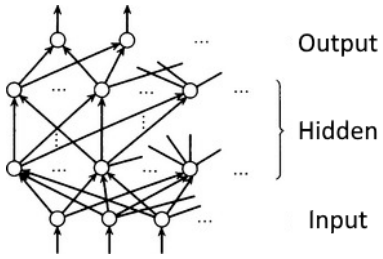

Figure 4.8: A schematic of a feedforward ANN structure. Adapted from Anzai [9].

For this method a new data set of 172 points is obtained via LHS, with the three powertrain design variables included. A test set of 5 points is taken from the data set. In Matlab, a neural network is created and trained using the remaining data to predict the fuel burn mass. In this case one of each type of layer are used, and 'Bayesian regularization backpropagation' is selected as training algorithm. The number of nodes in the hidden layer is to be determined for the ANN fit. It is varied from 5 to

[1] https://www.mathworks.com/matlabcentral/fileexchange/10056-scattered-data-interpolation-and-approximation-using-radial-base-functions, visited on 25/09/2020.

20, and the sum of the maximum and relative errors found from the test set is calculated. For each number of nodes in the hidden layer, the training is repeated 5 times since each time it is different. This entire process is repeated 4 times in total, with each time a different test set is taken from the data set. The result can be seen in Figure 4.9.

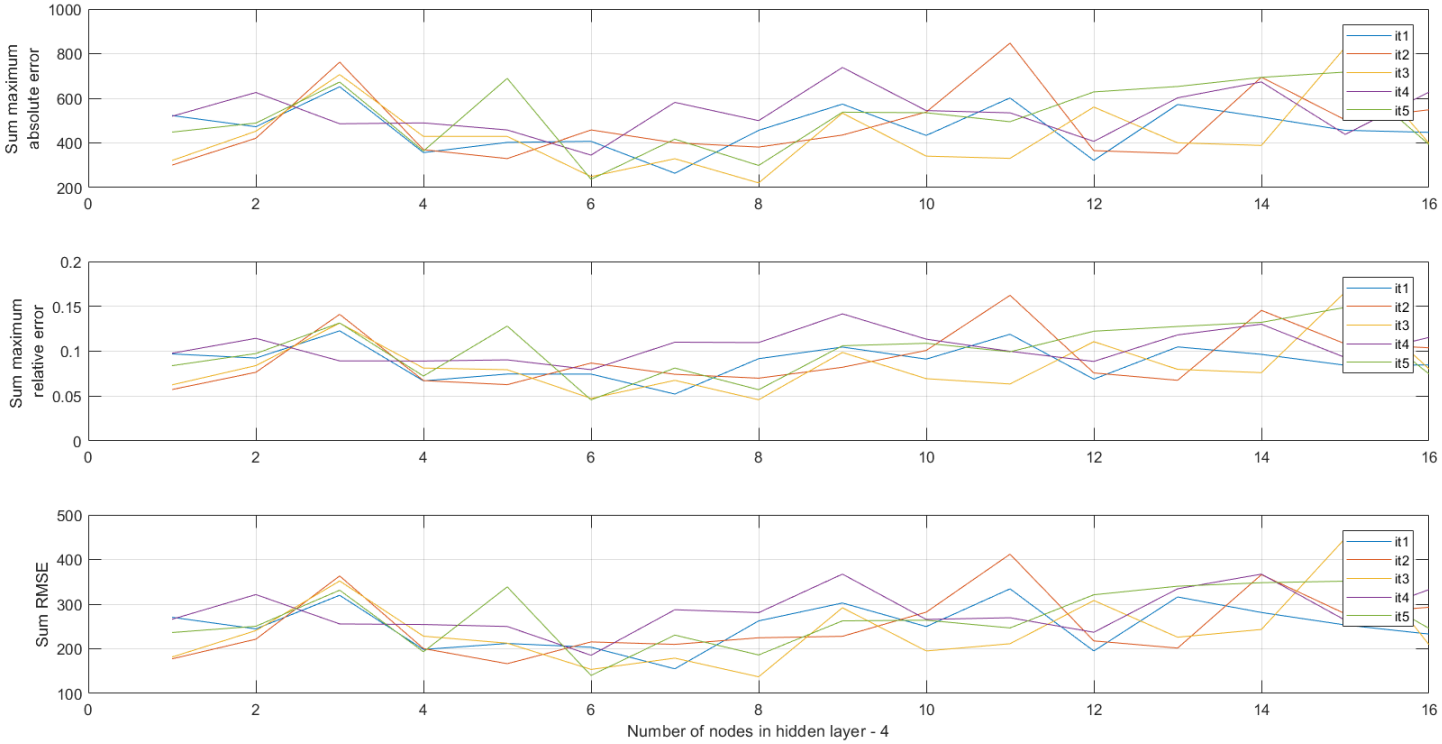

Figure 4.9: The sum of errors of the fuel burn prediction for the A320neo using ANN.

The selected number of nodes in the hidden layer is 12 since it gives the smallest sum of errors. The ANN fit is then used as a fuel burn prediction model for the A320neo. It is tested on the result of the powertrain optimum from Section 4.1.1, and its predicted value deviates 0.32% from the actual value of -3.1%. The optimization problem is formulated as follows:

$$
\begin{aligned}
\min_{x} \quad & f(x) = m_{f,burn}(x) \\
\text{subject to} \quad & 0 < \phi_{TO}[-] < 0.3 \quad 0 < \phi_{Cl}[-] < 0.3 \quad 88 < s_{en}[\%] < 95 \\
& 4 < c_r[m] < 10 \quad 4.5 < b_i[m] < 10 \quad 15 < \Lambda_i[deg] < 35 \\
& 6 < b_o[m] < 16 \quad 0.75 < c_t[m] < 3
\end{aligned}
$$

The optimizaion is performed with 'fmincon' using the reference A320neo as starting point. An optimum point is found at 3861 kg of fuel burn, which is a -20.1% difference with respect to the reference. The optimum point is then re-evaluated using MASS, of which the results are provided in Table 4.11.

Table 4.11: The result of the powertrain and planform optimization of the A320neo.

	ϕ_{TO} [-]	ϕ_{Cl} [-]	s_{en} [%]	c_r [m]	b_i [m]	Λ_i [deg]	b_o [m]	c_t [m]	$m_{f,burn}$ [kg]
Reference	0	0	100	7.1	6.35	22.24	11.25	1.375	4836
Optimum	0.21	0.3	88	4.0	7.46	35	15.6	0.75	4018

The optimum is found at a point where many of the design variables reach their bounds. The fuel burn change with respect to the reference A320neo is calculated to be -16.9%. It appears that the surrogate model is less accurate nearby boundary points. Therefore it is recommended to sample the design space around the found optimum, and optimize with the newly obtained surrogate model. However, the current optimum point is expected and logical. The planform design tends to maximize the inner sweep and the aspect ratio. The former leads to reduced wave drag, whereas the latter leads to reduced induced drag. The change of the drag polar for cruise is depicted in Figure 4.10.

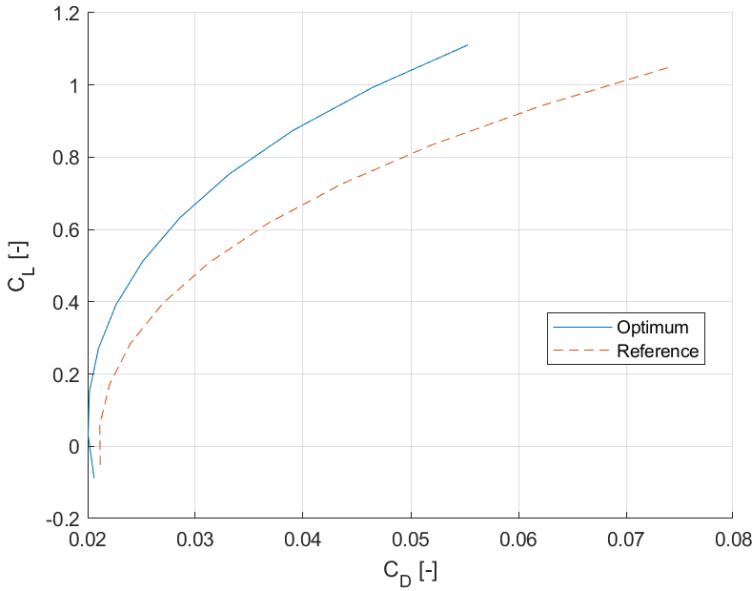

Figure 4.10: The reference and the optimized A320neo drag polars at M = 0.78, h = 35 kft, S_{ref} = 129 m^2.

The powertrain variation is directed towards minimum engine core scaling, which is made possible when higher values of ϕ are reached. The resultant mass reduction is tabulated in Table 4.12, under Δm_{en}. In the same table it can be seen that the battery mass, m_{bat}, causes the majority of the total mass increase. Note that m_{bat} is included in the mass of additional electrical systems due to HEP, $m_{el,HEP}$. By adding $m_{el,HEP}$ (10616 kg) and Δm_{en} (-502 kg) to the reference m_{OE} (44901 kg), the resulting m_{OE} is 55015 kg which is 35 kg higher than m_{OE} at the optimum. This means that the airframe variation has reduced the weight by 35 kg.

Table 4.12: The selected masses of the reference and optimized A320neo.

	m_{TO} [kg]	m_{OE} [kg]	$m_{el,HEP}$ [kg]	m_{bat} [kg]	Δm_{en} [kg]
Reference	68452	44901	0	0	0
Optimum	77713	54980	10616	7723	-502

The estimated contributions of the individual design variables to the fuel burn reduction are put in Table 4.13. The reported values are based on the figures from B that have been obtained prior to the optimization. Those figures display the fuel burn changes for variations of the individual design variables around the reference design. Therefore the tabulated numbers are only indicative. In this case, the most influential parameters are the chord and sweep angle of the wing inner section. That shows that airframe changes have a larger share in fuel burn reduction than HEP changes.

Table 4.13: The contributions to the fuel burn reduction by the A320neo parameters at their optimum values.

Parameter	Fuel burn change at optimum value [%]
ϕ_{TO}	1.74
ϕ_{Cl}	1.46
s_{en}	-1.88
c_r	-10.3
b_i	1.38
Λ_i	-5.74
b_o	-0.71
c_t	-0.87

The optimum does not lie at the boundary of the design space, but it is suggested to include constraints to check for feasibility. For example, one could include engine operation limits, aeroelastic effects, stability and controllability characteristics, and take-off and landing requirements.

4.2. Blended Wing-Body

The BWB, which is equivalent to the A320neo, is modeled based on the documentation from Brown [51]. The resulting model is depicted in Figure 4.11.

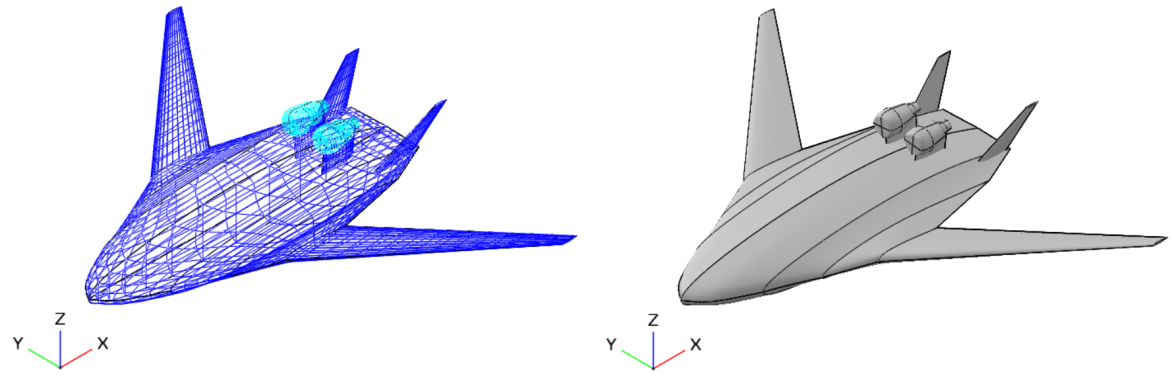

(a) The BWB with a wireframe surface.

(b) The BWB with a shaded surface.

Figure 4.11: The two generated views of the A320neo-equivalent BWB.

The aerodynamics have been compared with the reference, see Figure 4.12. The predicted zero-lift drag comes close to the reference. At higher lift the discrepancy becomes more apparent, which is for one part caused by the overestimated wave drag. The airfoil at the inner section is not known hence an airfoil is guessed based on the drawings. That also contributes to the difference in drag at higher lift.

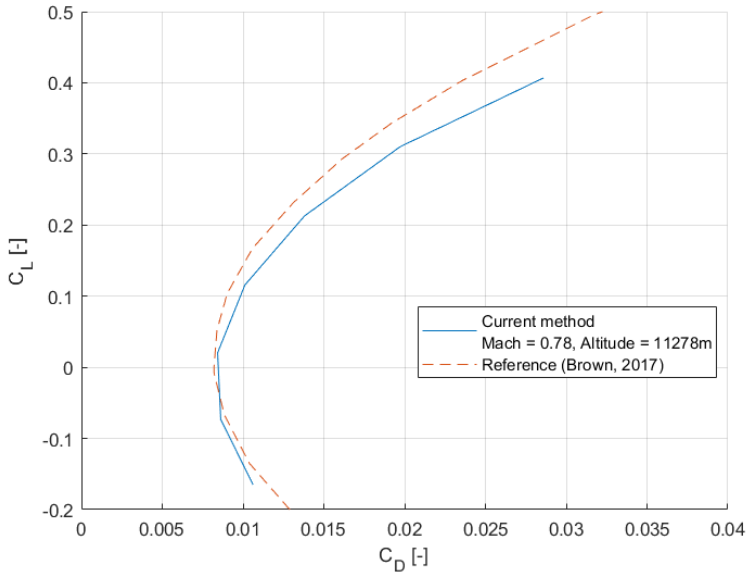

Figure 4.12: The reference and the calculated BWB drag polars.

The weight formulae for the wing and fuselage have been tailored to the BWB design using Howe's method [52]. The weight breakdown is shown with the reference in Table 4.14. There are significant differences between individual weight components, which are due to differences in the model. For example, MASS uses CFM LEAP engines whereas the reference uses engines that are tailored to its design. Differences in wing and fuselage weight occur due to the difference in mission. The current BWB is simulated for a shorter range mission, causing its all-up mass (and wing and fuselage masses) to be smaller than the reference's. In fact, the BWB in this study uses the same mission as described for the A320neo in Table 4.1. The difference in masses of systems, furnishings, and operational items is likely due to the difference in the way how mass increments are grouped.

Table 4.14: The BWB weight breakdown comparison.

Component	**Method**	**m**$_{computed}$ [kg]	**m**$_{ref}$ [kg] [51]	**Difference [%]**
Wing	Howe	2429	3816	-36.3
Fuselage	Howe	11351	13176	-13.9
Vertical tail	Kundu	690	432	59.7
Landing gear	Torenbeek	2440	2448	-0.32
Propulsion	Kundu	9980	6840	45.9
Systems	Torenbeek	4556	3384	34.6
Furnishings	Torenbeek	3350	4824	-30.6
Operational items	Torenbeek	4168	3240	28.6
OEW	Summation	38965	38088	2.30

4.2.1. BWB Powertrain Variations

The powertrain of the BWB is varied in the same way as described for the A320neo in Section 4.1.1. A design of experiments is performed for the powertrain design variables s_{en}, ϕ_{TO}, and ϕ_{Cl}. The parameter of interest is the fuel burn change of the HEP variant with respect to its non-HEP counterpart. The bounds and step sizes of the design variables are tabulated in Table 4.15. The resulting contour plots of the fuel burn change of the BWB can be seen in Figure 4.13.

Table 4.15: The bounds and step sizes of the design variables used for the design of experiments of the HEP BWB.

	ϕ_{TO} [-]	ϕ_{Cl} [-]	s_{en} [%]
Lower bound	0	0	85
Upper bound	0.3	0.3	95
Step size	0.03	0.03	1

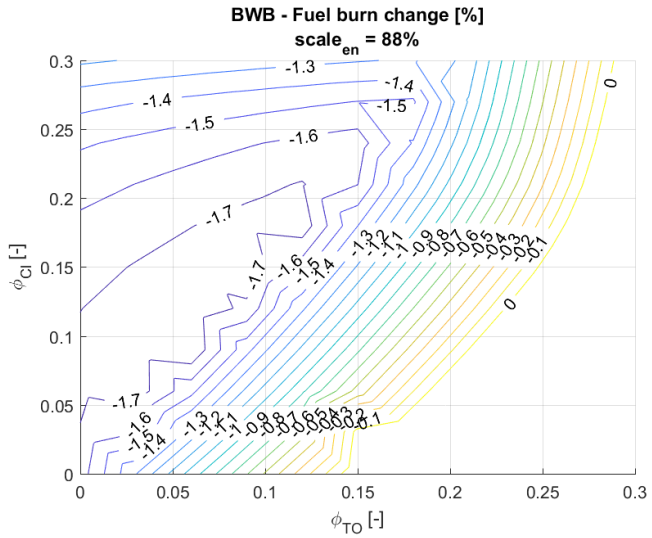

(a) s_{en} = 88%

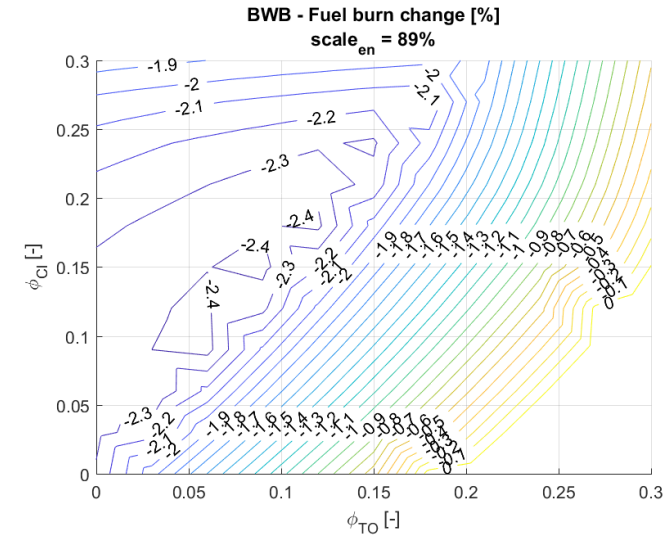

(b) s_{en} = 89%

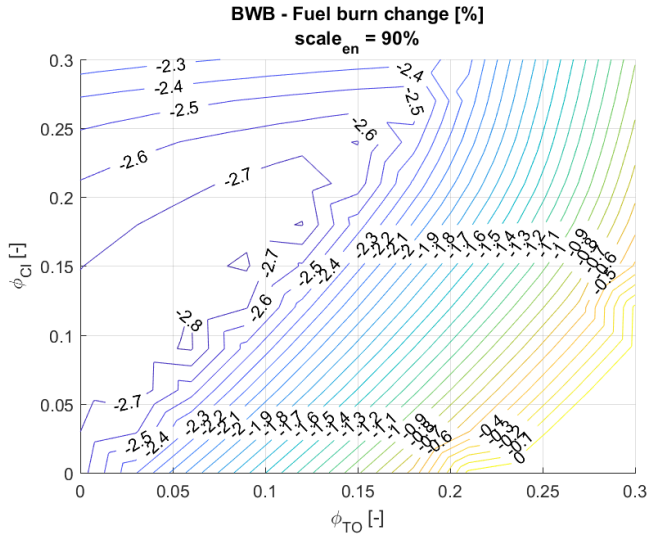

(c) s_{en} = 90%

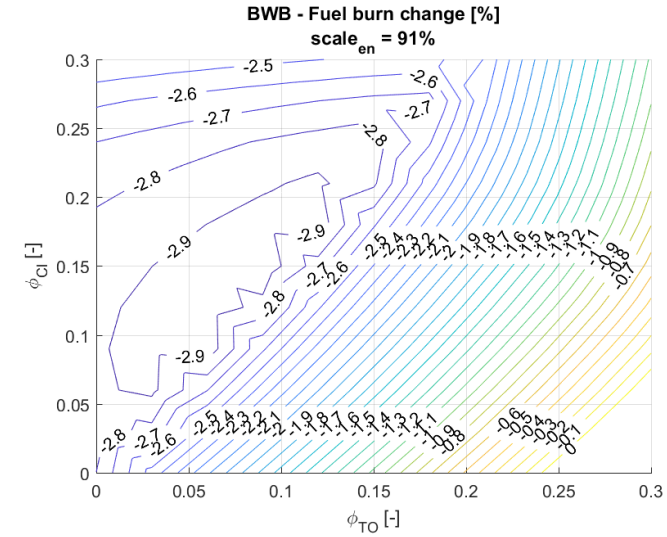

(d) s_{en} = 91%

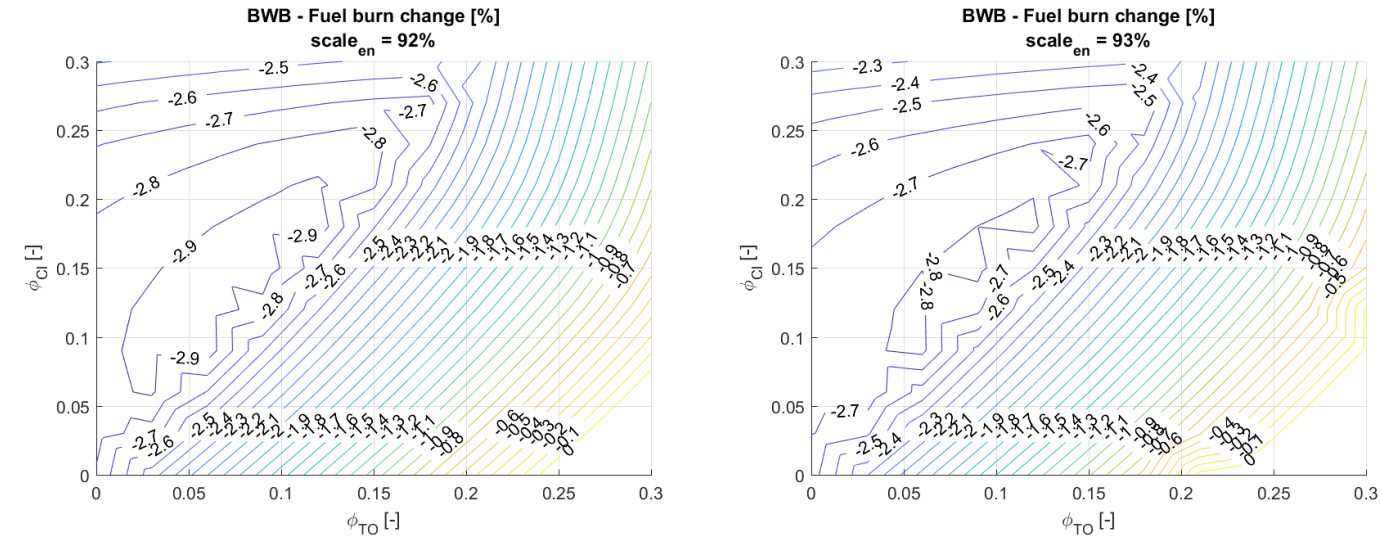

(e) s_{en} = 92%

(f) s_{en} = 93%

Figure 4.13: The contour plots of the fuel burn change of the HEP BWB with respect to the non-HEP variant.

Not all contour plots are shown in the figure since the omitted plots display higher fuel burn changes which are irrelevant. The minimum fuel burn change seems to reach its limit at -2.9% as seen for s_{en} = 91% and 92% (Figures 4.13d and 4.13e respectively). There also appears to be three stationary points, judging from the -2.4% areas in Figure 4.13b. These points also appear in Figures 4.13c and 4.13f, so it is safe to assume that these are also present for the other values of s_{en} within the design space.

The next step is to perform the optimization with 'fmincon' on the following problem:

$$\begin{aligned} \min_{x} \quad & f(x) = m_{f,burn}(x)/m_{f,burn,0} - 1 \\ \text{subject to} \quad & 0.05 < \phi_{TO} < 0.15 \\ & 0.05 < \phi_{Cl} < 0.2 \\ & 91\% < s_{en} < 92\% \end{aligned}$$

To find the coordinates of the three stationary points, the starting point of the solver is set in close proximity of each. The results of the optimizations can be found in Table 4.16.

Table 4.16: The result from the BWB HEP optimization.

	ϕ_{TO} [-]	ϕ_{Cl} [-]	s_{en} [%]	f [%]
$x_{opt,1}$	0.093	0.140	91.4	-3.03
$x_{opt,2}$	0.064	0.096	91.5	-3.02
$x_{opt,3}$	0.122	0.184	91.5	-3.02

As can be seen in Table 4.16, a minimum of -3.03% fuel burn change can be obtained with HEP variations for the BWB. That corresponds with optimum number 1. However, the differences between the optima are very small and one may argue that they are negligible. A remarkable finding is that virtually the same optimum value can be found for diverse combinations of ϕ. Since the optimization is unconstrained, feasibility checks should be performed to limit the design space. Nonetheless, the ϕ values are within the expected feasible region so the three optima may all be viable.

4.2.2. BWB Powertain and Geometry Variations

The optimization for minimal fuel burn of the BWB using powertrain and planform variations is done in a similar way as for the A320neo. Compared with the A320neo, there are fewer steps for the BWB since the methods that have not succeeded before are not repeated. The steps taken are as follows:

1. Determine the design variables;
2. Perform design of experiments for surrogate modeling;
3. Train an ANN to serve as a fuel burn prediction model;
4. Run surrogate optimization for minimal fuel burn.

The same three powertrain design variables are used as described in Section 4.2.1. The planform design variables are selected based on the parameterization that is depicted in Figure 4.14. The shown parameters capture the overall shape of the aircraft. The 7 planform design variables are: c_i, b_i, b_o, c_r, c_t, Γ, and Λ. The shape of the inner section is preserved as c_i also rescales that section along the x-axis. The optimization problem for the BWB is formulated as follows:

$$
\begin{aligned}
\min_{x} \quad & f(x) = m_{f,burn}(x) \\
\text{subject to} \quad & 0 < \phi_{TO}[-] < 0.3 \qquad 0 < \phi_{Cl}[-] < 0.3 \qquad 88 < s_{en}[\%] < 95 \\
& 20 < c_i[m] < 35 \qquad 4 < b_i[m] < 10 \qquad 8 < b_o[m] < 15 \\
& 3 < c_r[m] < 8 \qquad 0.5 < c_t[m] < 3 \qquad -4 < \Gamma[deg] < 4 \\
& 35 < \Lambda[deg] < 60
\end{aligned}
$$

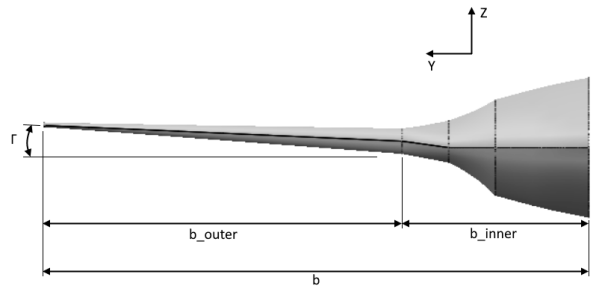

(a) The front view of the BWB planform.

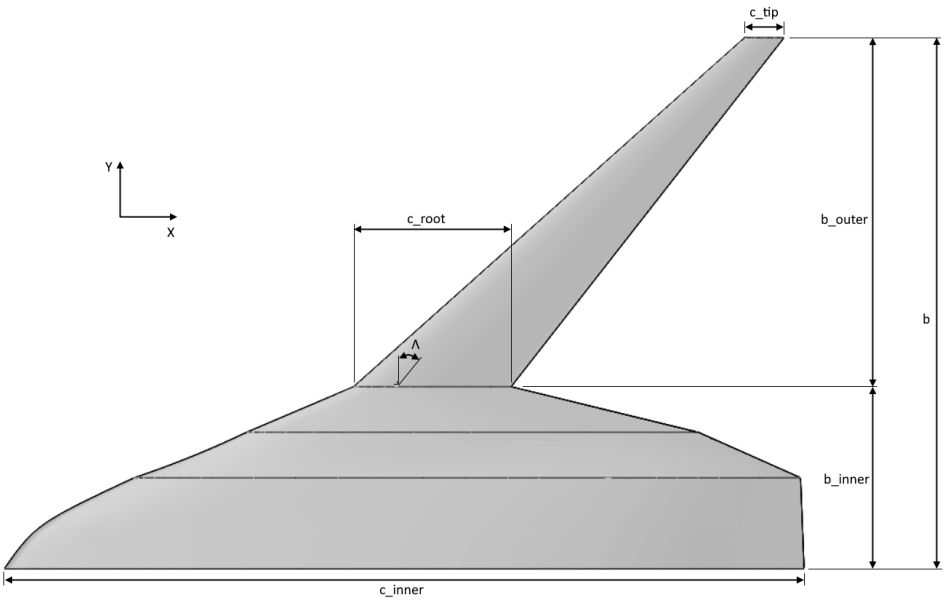

(b) The top view of the BWB planform.

Figure 4.14: An overview of the geometry variables of the BWB.

The data for the surrogate model is obtained using LHS, which fall within the boundaries stipulated in the optimization problem formulation. Furthermore, the data obtained from earlier design of experiments (see Section 4.2.1) is added, resulting in a total number of samples of 1200. The ANN set-up and training process is the same as described in Section 4.1.2, except that there are 12 samples in the test set. The sum of the errors obtained using the test set are visualized in Figure 4.15. It appears that 10 nodes in the hidden layer yield the lowest error, which is chosen for the ANN model. The ANN model is then tested on the powertrain optimum found in Section 4.2.1. The difference between the predicted and actual value of the fuel burn change is 0.4%. The optimum fuel burn change after powertrain and geometry optimization is expected to be in the range between -10% to -20%, judging from the result of the A320neo optimization.

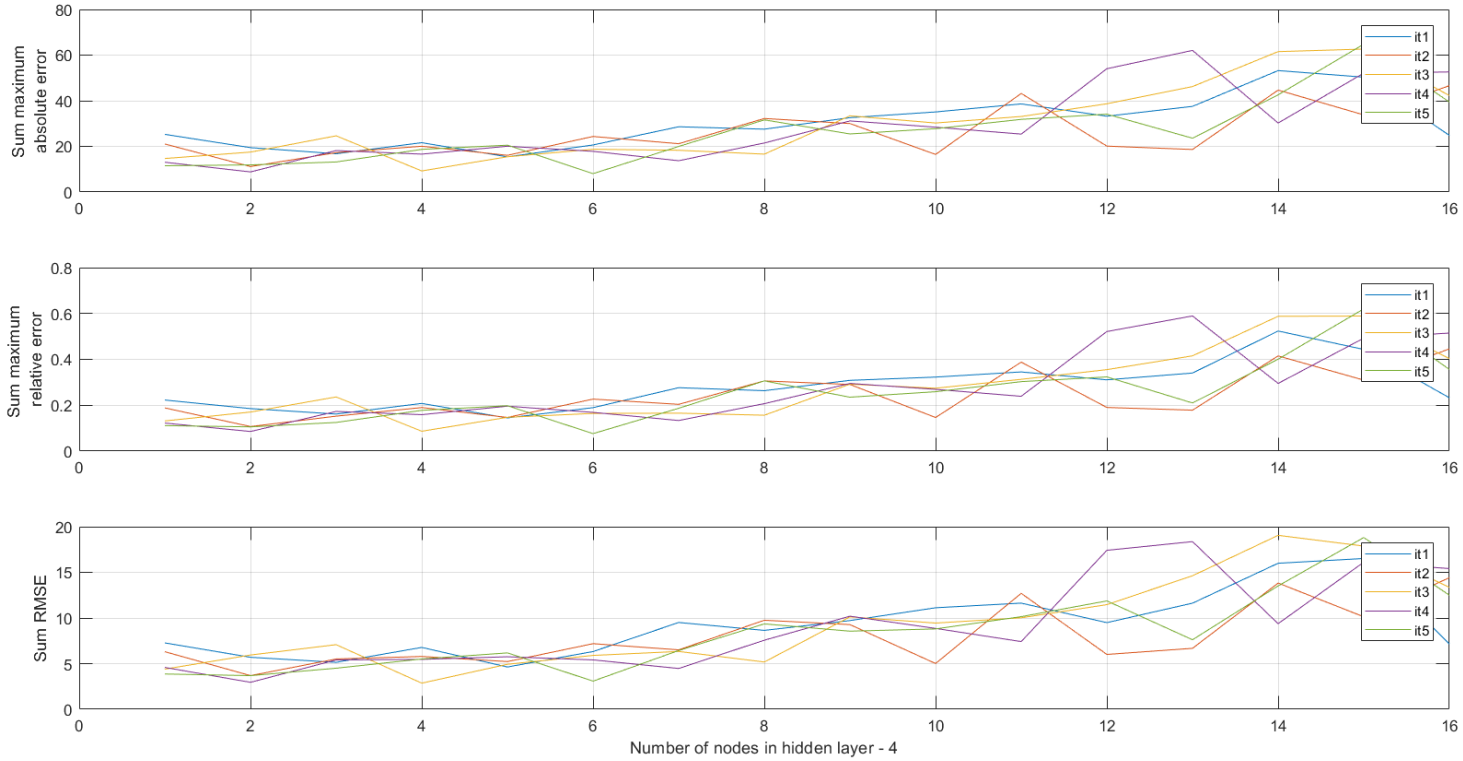

Figure 4.15: The sum of errors of the fuel burn prediction for the BWB using ANN.

The function 'fmincon' is used to find the optimum for the BWB. The optimum fuel burn reduction with respect to the reference BWB is 31.9%. The optimum point is provided to MASS for re-evaluation, resulting in a -13.8% fuel burn change. Also for the BWB the surrogate model is less accurate at predicting fuel burn when several design variables are at their boundaries. The results are put in Table 4.17 together with the reference (starting) values.

Table 4.17: The results of the BWB powertrain and planform optimizations for minimal fuel burn.

	ϕ_{TO} [-]	ϕ_{Cl} [-]	s_{en} [%]	c_i [m]	b_i [m]	b_o [m]	c_r [m]	c_t [m]	Γ [deg]	Λ [deg]	$m_{f,burn}$ [kg]
Reference	0	0	100	26.4	6.0	11.5	5.2	1.3	0	48.3	4492
Optimum	0	0	90.1	20	4	13.3	3	0.5	-1.4	36.5	3872

As seen before in Section 4.1.2, the planform changes to increase the aspect ratio which then decreases the induced drag. The evidence for that is that the chord lengths have gone down to their lower bounds and the outer span has extended. However, the inner span has shortened. This is because the inner section of the wing acts as the fuselage and therefore has a large surface area. The shorter inner span leads to a smaller surface area and thus a smaller parasite drag. In fact, the reduction in parasite drag (over)compensates for the increase in induced drag. The dihedral angle is slightly decreased with respect to its original position. Even though the original position says the dihedral is 0 deg, the reality is that the wing is already tilted upwards towards the tip (see Figure 4.14a). The original wing is set to that position using other parameters so that the dihedral parameter remains 0. The decrease in dihedral means that the span is slightly increased, which decreases the induced drag. The reduction in outer wing sweep occurred since the fuel saving effect of the weight decrease is stronger than the increased wave drag. The drag polars of the reference and optimized designs are portrayed in 4.16.

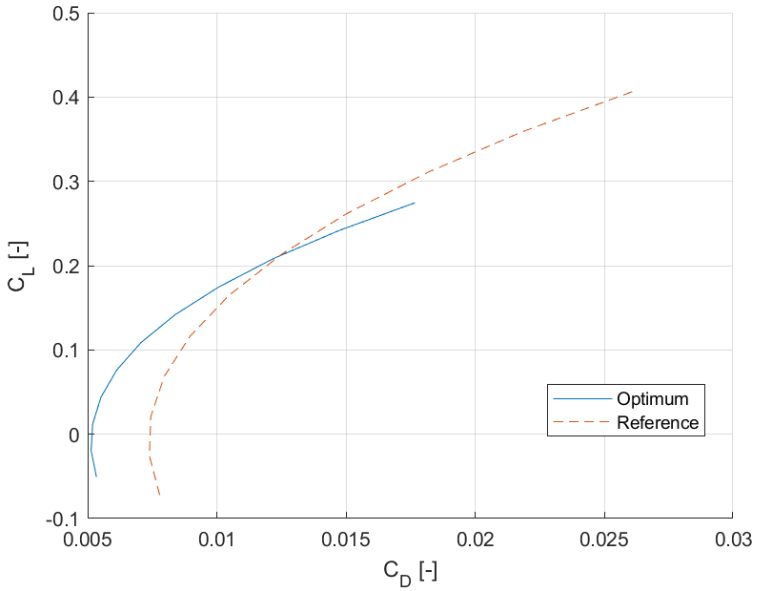

Figure 4.16: The reference and the optimized BWB drag polars at M = 0.78, h = 35 kft, S_{ref} = 308 m^2.

Regarding the powertrain variables, it is not surprising that both ϕ's are zero. The improvements in drag and mass lead to a level of required thrust where the downscaled engine core does not need any additional power support. The mass reduction due to engine core downscaling, Δm_{en}, is captured in Table 4.18. It can be seen in the same table that the reduction of m_{OE} is primarily caused by the smaller airframe, as there are no batteries and accompanying systems present.

Table 4.18: The selected masses of the reference and optimized BWB.

	m_{TO} [kg]	m_{OE} [kg]	$m_{el,HEP}$ [kg]	m_{bat} [kg]	Δm_{en} [kg]
Reference	62172	38965	0	0	0
Optimum	55666	33083	0	0	-405

To shed light on the fuel burn reduction contributions of the individual design variables, Table 4.19 is added. The values are obtained in the same manner as for the A320neo described in Section 4.1.2. As seen before for the A320neo, the BWB's inner section variables also appear to contribute the most to the fuel burn reduction. This is expected since those variables size a major part of the aircraft and are allowed to deviate up to 33% from their original values. The powertrain change leads to a relatively small reduction in fuel burn compared to the planform changes.

Table 4.19: The contributions to the fuel burn reduction by the BWB parameters at their optimum values.

Parameter	Fuel burn change at optimum [%]
ϕ_{TO}	0
ϕ_{Cl}	0
s_{en}	-1.88
c_i	-5.79
b_i	-4.90
b_o	-1.08
c_r	-0.59
c_t	-0.76
Γ	-0.09
Λ	-1.91

It is suggested to add feasibility checks and certification requirements as constraints to the optimization problem. Few of them have already been mentioned at the end of Section 4.1.2.

4.3. Summary of Results

In this section all the results from the earlier optimizations are gathered in one overview. The fuel burn optima of the A320neo are summarized in Table 4.20 and likewise for the BWB in Table 4.21.

Table 4.20: The results of the fuel burn optimizations of the A320neo. Optimum 1 refers to powertrain variations only. Optimum 2 refers to powertrain and planform variations.

	ϕ_{TO} [-]	ϕ_{Cl} [-]	s_{en} [%]	c_r [m]	b_i [m]	Λ_i [deg]	b_o [m]	c_t [m]	$m_{f,burn}$ [kg]	$\Delta m_{f,burn}$ [%]
Reference	0	0	100	7.1	6.35	22.24	11.25	1.375	4836	0
Optimum 1	0.035	0.070	91.6	7.1	6.35	22.24	11.25	1.375	4686	-3.1
Optimum 2	0.21	0.3	88	4.0	7.46	35	15.6	0.75	4018	-16.9

Table 4.21: The results of the fuel burn optimizations of the BWB. Optimum 1 refers to powertrain variations only. Optimum 2 refers to powertrain and planform variations.

	ϕ_{TO} [-]	ϕ_{Cl} [-]	s_{en} [%]	c_i [m]	b_i [m]	b_o [m]	c_r [m]	c_t [m]	Γ [deg]	Λ [deg]	$m_{f,burn}$ [kg]	$\Delta m_{f,burn}$ [%]
Reference	0	0	100	26.4	6.0	11.5	5.2	1.3	0	48.3	4492	0
Optimum 1	0.093	0.140	91.4	26.4	6.0	11.5	5.2	1.3	0	48.3	4356	-3.0
Optimum 2	0	0	90.1	20	4	13.3	3	0.5	-1.4	36.5	3872	-13.8

Although limited, the implementation of HEP retrofits lead to fuel burn reductions for both A320neo and BWB. The expected fuel burn reductions are up to 3.1%, which are attributed to engine core downscaling. Even more fuel can potentially be saved when planform variations are included. The A320neo's airframe variation has led to a significant reduction in drag of more than 20% at cruise, and a small reduction in airframe weight of 35 kg. The major contributors are the root chord and inner sweep angle, as is evident from Table 4.13. The BWB achieves fuel burn reduction mostly by having a smaller inner section. The total effects are the take-off mass reduction of 10.5% and the improvement of around -33% in zero-lift drag. The most influential parameters are the inner section variables of chord and span, as can be seen in Table 4.19.

Furthermore, the BWB consistently shows a lower fuel burn than the A320neo. The reference BWB has a lower fuel burn mass than the HEP optimized A32neo, which implies that a configuration change can be more beneficial than only implementing parallel HEP in terms of fuel savings. If the two extremes of fuel burn masses are compared, i.e. the reference A320neo and the BWB's optimum 2, then a maximum of 19.9% fuel mass can be saved. In a study, where an A320neo is compared with its BWB equivalent design with varying centerbody mass, fuel burn gains are seen from 6 to 20% [53]. The fuel burn reductions seen here are of the same magnitude.

Conclusions & Recommendations

Conclusions

The aim of the research is to quantify the potential reductions in trip fuel that can be achieved with hybrid electric aircraft (HEA) by aircraft concept variations. A parallel hybrid electric propulsion (HEP) aircraft mission analysis framework called 'MASS' has been used to achieve that. This framework is found to feature all relevant disciplines to assess, among others, the fuel consumption of HEA at conceptual level. Those disciplines are captured in interlinked modules that cover the following aspects: mission, aircraft model, engine model, HEP model, and electric components model.

The introduction of HEP has led to newer aircraft concepts which have the potential to further reduce the fuel and energy consumption. MASS, however, did not have the capability to capture concept variations. To overcome that shortcoming, the framework has been extended with the ability to predict aircraft level aerodynamics and weight of varying aircraft designs. A working methodology has been determined to be a drag build-up method for the aerodynamics. For the weight prediction, the appropriate method is the summation of individual component weights obtained via formulas from different sources. The validation of the methodology is limited to available aircraft data. The suitable reference aircraft are considered to be the A320ceo and CSR-01. The drag prediction deviates up to 7.3% from the reference. Moreover, the operational empty weight varies less than 1% from the reference. MASS is then used to look further into the fuel economy of large passenger aircraft (LPA) subjected to (hybrid electric) powertrain and geometry variations.

The A320neo serves as the reference aircraft in this research due to its wide use. The A320neo has been modeled and assigned a short range mission of 800 nm with 150 pax. The aircraft then undergoes HEP and geometry variations to quantify how much trip fuel can be saved. The HEP variations concern the engine core downscaling and the accompanying electric power support to the engine, represented by the power split ϕ. The geometry variation is twofold: one is the change in planform and the other is the change in configuration from tube-and-wing (TAW) to blended wing-body (BWB).

The TAW configuration with HEP and planform variations allows up to 16.9% fuel burn reduction. The HEP-only optimization enables a fuel burn reduction of at most 3.1%. The planform changes have more potential to reduce fuel burn than applying a (parallel) HEP retrofit. For TAW, the weight reduction due to varying planform is insignificant. The fuel burn reduction stems mostly from the aerodynamic benefit. The cruise drag is reduced by at least 20%. The parameters that contributed the most to the fuel burn reduction are related to the inner wing section. The root chord and inner sweep angle can individually reduce up to 10% and 5.7% fuel burn respectively.

The BWB with HEP and planform variations can reduce its fuel consumption by 13.8%. The optimization with only the powertrain leads to a maximum fuel burn change of -3.0%. The planform change has again more influence on the fuel burn than HEP. In contrast to the TAW, both take-off weight and drag are reduced in this case. The former is reduced by 10.5% and the latter by at most 33%. The optimum BWB has a downscaled engine core without ϕ due to those improvements. The main determinants of trip fuel are in this case the inner section variables, as the inner wing also acts as fuselage. The inner chord and span can reduce up to 5.8% and 4.9% fuel respectively.

It is certain that geometry variations on top of powertrain variations reduce more fuel consumption. If the non-HEP A320neo is changed to a fully optimized BWB, a maximum of 19.9% fuel burn reduction can be attained. It is observed that planform variations have a consistently larger effect on fuel burn reduction than HEP variations. Additionally, the BWB consistently displays lower fuel burn than the A320neo. Thus, one may consider to implement configuration changes first before HEP retrofitting.

Recommendations

A number of recommendations can be made regarding the research, which are shown in the list below:

- Addition of feasibility checks
  The optimizations that have been performed were unconstrained. That has led to significant fuel burn reductions and raises the question which part of the design space is feasible. Since the optimizer leans towards maximum aspect ratio designs, i.e. maximum span and minimum chord length, a constraint can be used relating to aeroelastic effects such as flutter. Other suggested constraints to add are: take-off and landing requirements, stability and controllability characteristics, and engine operating limits.

- Mission optimization for specific configurations
  Only one mission has been simulated in the analyses. It would be interesting to see how much fuel can be saved if the mission and flight trajectory would be optimized for each aircraft geometry and/or powertrain variation.

- Improvement of the wave drag estimation method
  The current wave drag estimation method overpredicts this drag component. Therefore a different method should be implemented. A promising method seems to be the 'Delta method', which is an empirical method. However, it is uncertain whether this method can be used for unconventional designs such as blended wing-bodies, truss-braced wings, or Prandtl planes.

- Improvement of the component weight prediction
  The individual component weights can show significant deviations from the reference values, especially regarding the blended wing-body. Even though weight prediction models exist, this type of aircraft has not been produced for commercial flight before. The consequential lack of validation data is suggested to be remedied by designing it in much greater detail and putting it in production.

- Investigate design space around optimum
  The neural network-based surrogate model has reduced accuracy at points near or on the boundary of the design space. For the optima, many of the design variables reached their boundary values. Therefore is it suggested to resample the design space around those points and retrain the surrogate model for increased accuracy.

- Generalization of the aircraft modeling
  The current modeling approach is suitable for tube-and-wing and blended wing-body aircraft. It should be generalized such that other configurations can be modeled and analyzed as well. Examples are truss-braced wings and Prandtl planes.

- Implementation of other powertrain and HEP variants
  A parallel HEP architecture is used in this study. MASS could be extended with other architectures such as serial HEP so that distributed propulsion and boundary layer ingestion technologies can be analyzed.

Bibliography

[1] Airbus, *Global Market Forecast 2019-2038: Cities, Airports & Aircraft*, Tech. Rep. (2019).

[2] Boeing, *Commercial Market Outlook 2019–2038*, Tech. Rep. (2019).

[3] C. Pornet and A. T. Isikveren, *Conceptual design of hybrid-electric transport aircraft,* Progress in Aerospace Sciences **79**, 114 (2015).

[4] K. R. Antcliff and F. M. Capristan, *Conceptual Design of the Parallel Electric-Gas Architecture with Synergistic Utilization Scheme (PEGASUS) Concept,* in *AIAA AVIATION Forum* (American Institute of Aeronautics and Astronautics, Denver, Colorado, United States, 2017).

[5] P. Schmollgruber, D. Donjat, M. Ridel, I. Cafarelli, O. Atinault, C. François, and B. Paluch, *Multi-disciplinary design and performance of the ONERA Hybrid Electric Distributed Propulsion concept (DRAGON),* in *AIAA SciTech Forum* (American Institute of Aeronautics and Astronautics, Orlando, FL, United States, 2020).

[6] W. F. Lammen and W. J. Vankan, *Energy Optimization of Single Aisle Aircraft with Hybrid Electric Propulsion,* in *AIAA SciTech Forum* (American Institute of Aeronautics and Astronautics, Orlando, FL, United States, 2020).

[7] National Academies of Sciences, Engineering, and Medicine, *Commercial Aircraft Propulsion and Energy Systems Research: Reducing Global Carbon Emissions* (The National Academies Press, Washington, DC, 2016).

[8] J. Quitter, M. Marino, and J.-M. Bauschat, *Highly Non-Planar Aircraft Configurations: Estimation of Flight Mechanical Derivatives Using Low-Order Methods,* (Darmstadt, Germany, 2019).

[9] Y. Anzai, *Pattern Recognition and Machine Learning* (Morgan Kaufmann, 2012).

[10] B. J. Brelje and J. R. R. A. Martins, *Electric, hybrid, and turboelectric fixed-wing aircraft: A review of concepts, models, and design approaches,* Progress in Aerospace Sciences **104**, 1 (2018).

[11] S. Sahoo, X. Zhao, and K. Kyprianidis, *A Review of Concepts, Benefits, and Challenges for Future Electrical Propulsion-Based Aircraft,* Aerospace **7**, 44 (2020).

[12] Airbus, *A320 Family Technology,* (2016).

[13] Anonymous, *Airbus A320,* (2020).

[14] Airbus, *Airbus Family Figures,* (2019).

[15] L. Jenkinson, P. Simpkin, and D. Rhodes, *Airbus Aircraft,* (2001).

[16] European Union Aviation Safety Agency, *Type Certificate Data Sheet No. EASA.A.064 for Airbus A318 -A319 - A320 - A321,* (2019).

[17] E. Obert, *Aerodynamic Design of Transport Aircraft* (IOS Press BV, Delft University Press, Amsterdam, Netherlands, 2009).

[18] A. Elham, *Weight Indexing for Multidisciplinary Design Optimization of Lifting Surfaces*, PhD thesis, Delft University of Technology, Delft, The Netherlands (2013).

[19] EAA, European Union Aviation Safety Agency, and Eurocontrol, *European Aviation Environmental Report 2019*, Tech. Rep. (2019).

[20] European Commission, *Flightpath 2050 Europe's Vision for Aviation, Report of the High Level Group on Aviation Research* (Publications Office of the European Union, Luxembourg, 2011).

[21] NASA, *Strategic Implementation Plan*, Tech. Rep. (2019).

[22] ACARE, *Strategic Research & Innovation Agenda,* (2017).

[23] M. K. Bradley and C. K. Droney, *Subsonic Ultra Green Aircraft Research: Phase II – Volume II – Hybrid Electric Design Exploration*, Contractor report (The Boeing Company, Huntington Beach, California, 2015).

[24] A. T. Isikveren, C. Pornet, P. C. Vratny, and M. Schmidt, *Optimization of Commercial Aircraft Utilizing Battery-based Voltaic-Joule/Brayton Propulsion,* Journal of Aircraft **54**, 246 (2016).

[25] M. Iwanizki, M. J. Arzberger, M. Plohr, D. Silberhorn, and T. Hecken, *Conceptual Design Studies of Short Range Aircraft Configurations with Hybrid Electric Propulsion,* in *AIAA AVIATION Forum* (American Institute of Aeronautics and Astronautics, Dallas, Texas, 2019).

[26] M. Voskuijl, J. Van Bogaert, and A. G. Rao, *Analysis and design of hybrid electric regional turboprop aircraft,* CEAS Aeronautical Journal **9**, 15 (2018).

[27] B. Aigner, E. Stumpf, A. Hinz, and R. W. De Doncker, *An Integrated Design Framework for Aircraft with Hybrid Electric Propulsion,* in *AIAA SciTech Forum* (American Institute of Aeronautics and Astronautics, Orlando, FL, United States, 2020).

[28] J. Gladin, D. Trawick, C. Perullo, J. C. M. Tai, and D. N. Mavris, *Modeling and Design of a Partially Electric Distributed Aircraft Propulsion System with GT-HEAT,* in *AIAA SciTech Forum* (American Institute of Aeronautics and Astronautics, Grapevine, Texas, United States, 2017).

[29] W. F. Lammen and W. J. Vankan, *Electrification studies of single aisle aircraft: A 'retrofit' investigation including parallel hybrid electric propulsion,* (2019).

[30] R. J. M. Elmendorp, R. Vos, and G. La Rocca, *A Conceptual Design and Analysis Method for Conventional and Unconventional Airplanes,* in *ICAS 2014* (St. Petersburg, Russia, 2014).

[31] T. W. Lukaczyk, A. D. Wendorff, M. Colonno, T. D. Economon, J. J. Alonso, T. H. Orra, and C. Ilario, *SUAVE: An Open-Source Environment for Multi-Fidelity Conceptual Vehicle Design,* in *AIAA AVIATION Forum* (Dallas, TX, United States, 2015).

[32] A. W. X. Ang, *Hybrid Electric Propulsion Systems Integrated performance analysis applied on short-range aircraft*, Master's thesis, TU Delft, Delft (2016).

[33] S. C. Tan, *Electrically Assisted Propulsion & Power Systems for Short-Range Missions. Electrification of a Conventional Airbus A320neo*, Master's thesis, TU Delft, Delft (2018).

[34] W. J. Vankan and W. F. Lammen, *Parallel hybrid electric propulsion architecture for single aisle aircraft - powertrain investigation,* in *MATEC Web of Conferences* (2019).

[35] C. Pornet, C. Gologan, P. C. Vratny, A. Seitz, O. Schmitz, A. T. Isikveren, and M. Hornung, *Methodology for Sizing and Performance Assessment of Hybrid Energy Aircraft,* Journal of Aircraft **52**, 341 (2015).

[36] L. Lorenz, A. Seitz, and H. Kuhn, *Hybrid Power Trains for Future Mobility,* (Stuttgart, Germany, 2013).

[37] AIAA, *Guidelines for Analysis of Hybrid Electric Aircraft System Studies: Nomenclature, Pictographic Representations, Standalone and Combined Properties and Attributes, Metrics, and Figures of Merit,* (2019).

[38] D. F. Finger, R. De Vries, R. Vos, C. Braun, and C. Bil, *A Comparison of Hybrid-Electric Aircraft Sizing Methods,* in *AIAA SciTech Forum* (American Institute of Aeronautics and Astronautics, Orlando, FL, United States, 2020).

[39] W. J. Fredericks, K. R. Antcliff, G. Costa, N. Deshpande, M. D. Moore, E. A. S. Miguel, and A. N. Snyder, *Aircraft Conceptual Design Using Vehicle Sketch Pad,* (American Institute of Aeronautics and Astronautics, Orlando, Florida, United States, 2010).

[40] Airbus, *A320 Aircraft Characteristics Airport and Maintenance Planning,* (2019).

[41] O. Gur, W. H. Mason, and J. A. Schetz, *Full Configuration Drag Estimation,* Journal of Aircraft **47** (2010), 10.2514/1.47557.

[42] S. F. Hoerner, *Fluid-Dynamic Drag: Practical Information on Aerodynamic Drag and Hydrodynamic Resistance* (Hoerner Fluid Dynamics, 1965).

[43] M. Drela, *Flight Vehicle Aerodynamics* (The MIT Press, Cambridge, Massachusetts, 2014).

[44] D. P. Raymer, *Aircraft Design: A Conceptual Approach*, AIAA Education Series (American Institute of Aeronautics and Astronautics, Washington, D.C., United States, 1992).

[45] P.-A. Tetrault, J. A. Schetz, and B. Grossman, *Numerical Prediction of Interference Drag of Strut–Surface Intersection in Transonic Flow,* AIAA JOURNAL **39** (2001), 10.2514/2.1389.

[46] T. M. Young, *Performance of the Jet Transport Airplane: Analysis Methods, Flight Operations, and Regulations* (Wiley, 2017).

[47] A. K. Kundu, *Aircraft Design* (Cambridge University Press, New York, 2010).

[48] E. Torenbeek, *Synthesis of subsonic airplane design* (Delft University Press, Delft, The Netherlands, 1982).

[49] J. Roskam, *Airplane Design: Preliminary sizing of airplanes* (DARcorporation, 1985).

[50] K. Risse, K. Schäfer, F. Schültke, and E. Stumpf, *Central Reference Aircraft data System (CeRAS) for research community,* CEAS Aeronautical Journal **7**, 121 (2016).

[51] M. T. H. Brown, *Conceptual Design of Blended Wing Body Airliners within a semi-automated design framework*, Master's thesis, TU Delft, Delft, The Netherlands (2017).

[52] D. Howe, *Blended wing body airframe mass prediction,* Proceedings of the Institution of Mechanical Engineers, Part G: Journal of Aerospace Engineering **215**, 319 (2001).

[53] A. Sgueglia, P. Schmollgruber, E. Benard, N. Bartoli, and J. Morlier, *Preliminary Sizing of a Medium Range Blended Wing-Body using a Multidisciplinary Design Analysis Approach,* in *MATEC Web of Conferences*, Vol. 233 (2018).

A

Project Gantt Chart

Gantt Chart

WBS	Name	Begin date	End date	Duration
1	Perform research design and literature study	02/12/19	31/01/20	45
1.1	Perform conceptual design	02/12/19	26/12/19	19
1....	Explore project context	02/12/19	10/12/19	7
1....	Decide on research objective	09/12/19	10/12/19	2
1....	Construct the research framework	10/12/19	12/12/19	3
1....	Formulate research questions	11/12/19	13/12/19	3
1....	Define concepts	12/12/19	16/12/19	3
1....	Reiterate conceptual design	16/12/19	26/12/19	9
1.2	Perform technical design	02/12/19	31/01/20	45
1....	Decide on research strategy	06/12/19	13/12/19	6
1....	Identify required research material	11/12/19	31/01/20	38
1....	Draw up a research planning	02/12/19	31/01/20	45
1.3	Reflect on research design and literature study	02/12/19	31/01/20	45
1.4	Deliver project plan	31/01/20	31/01/20	0
2	Write literature study report	02/12/19	30/04/20	109
2.1	Find and study literature	02/12/19	26/03/20	84
2.2	Deliver draft literature study report	13/01/20	13/01/20	0
2.3	Deliver literature study report	24/04/20	24/04/20	0
2.4	Present literature study	01/05/20	01/05/20	0
3	Main phase I: Tool design, verification and validation	30/12/19	17/04/20	80
3.1	Familiarize with aircraft modeling module	30/12/19	17/04/20	80
3.2	Integrate module within HEP analysis framework	24/02/20	17/04/20	40
3.3	Validate the framework	02/03/20	17/04/20	35
4	Main phase II: Performance optimization	20/04/20	16/06/20	42
4.1	Perform sensitivity studies using the framework	20/04/20	04/05/20	11
4.2	Perform optimization studies with the framework	05/05/20	16/06/20	31
4.3	Validate the results	18/05/20	16/06/20	22
5	Main phase III: Final evaluation	17/06/20	20/07/20	24
5.1	Draw conclusions based on results	17/06/20	20/07/20	24
5.2	Recommend future work	06/07/20	20/07/20	11
6	Write Mid-Term report	17/02/20	11/05/20	61
7	Deliver Mid-Term report	12/05/20	12/05/20	0
8	Perform Mid-Term review	25/05/20	25/05/20	0
9	Perform progress review	15/07/20	15/07/20	0
10	Main phase IV: Additional analysis	21/07/20	25/09/20	49
11	Modify Master's thesis	24/08/20	23/10/20	45
12	Deliver green light summary	12/10/20	12/10/20	0
13	Perform green light review	19/10/20	19/10/20	0
14	Deliver draft thesis	26/10/20	26/10/20	0
15	Finalize Master's thesis	26/10/20	20/11/20	20
16	Hand-in Master's thesis	23/11/20	23/11/20	0
17	Prepare for thesis defence	23/11/20	14/12/20	16
18	Defend Master's thesis	15/12/20	15/12/20	0

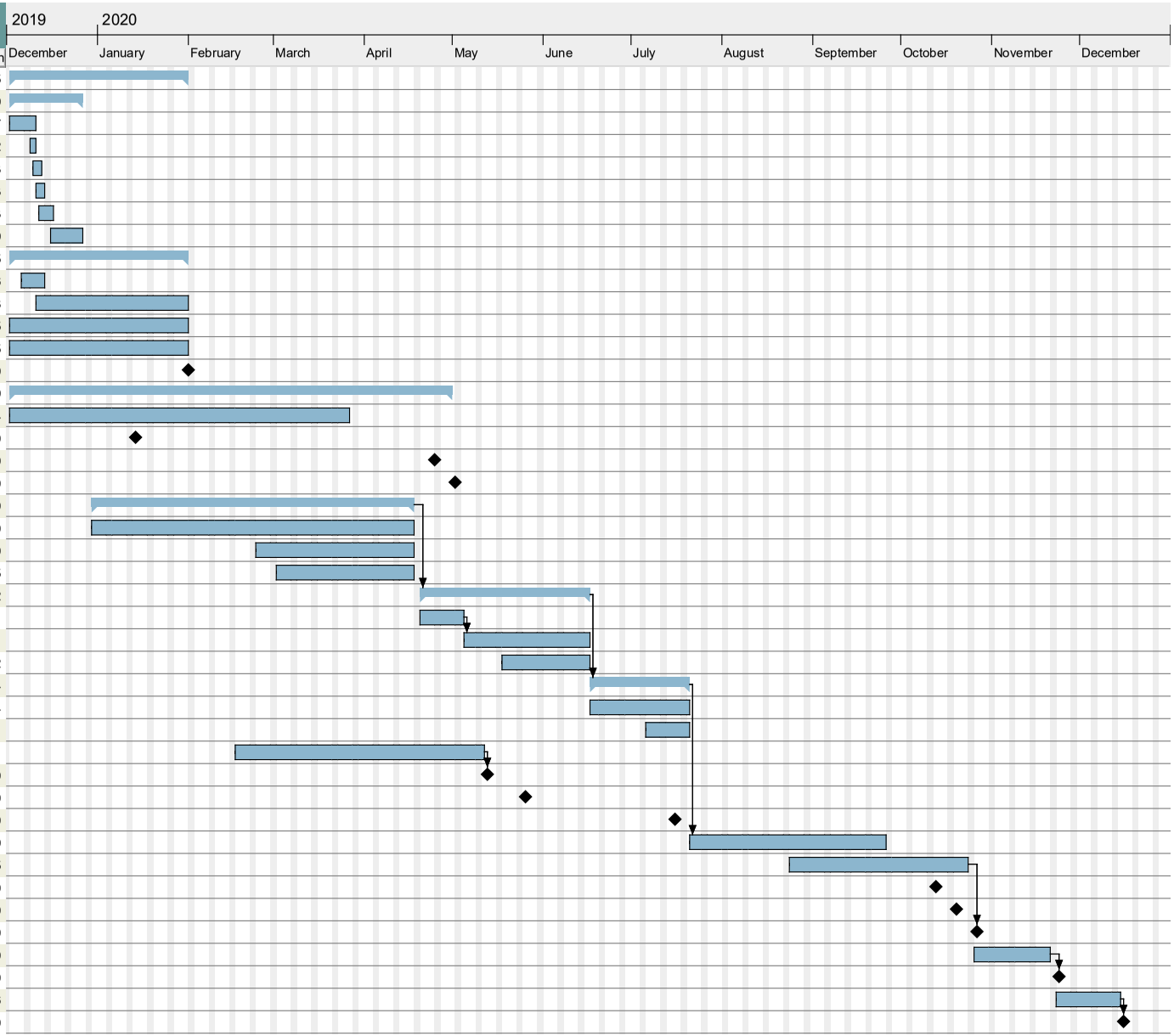

B

Fuel Burn Effects

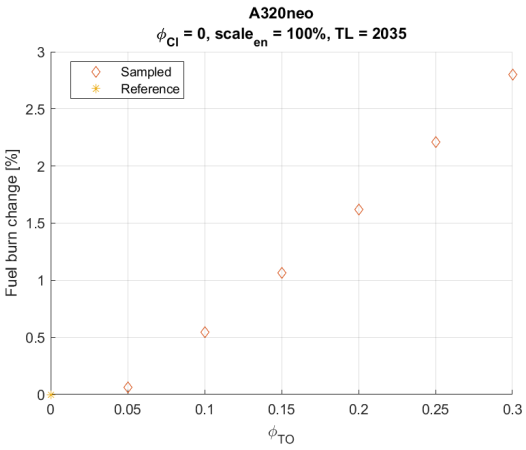

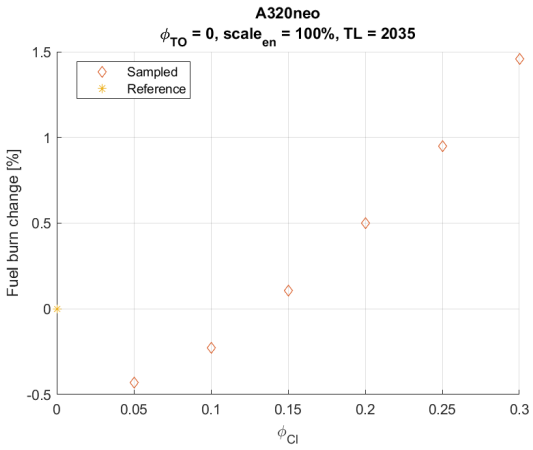

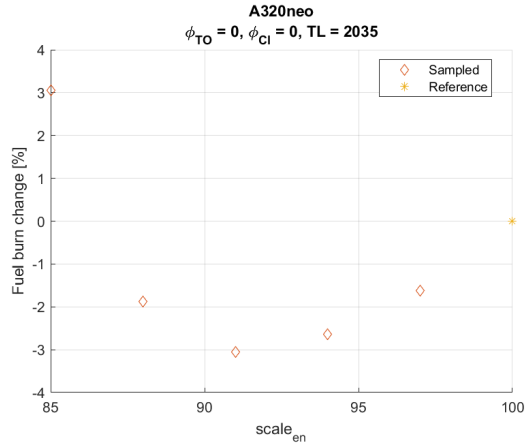

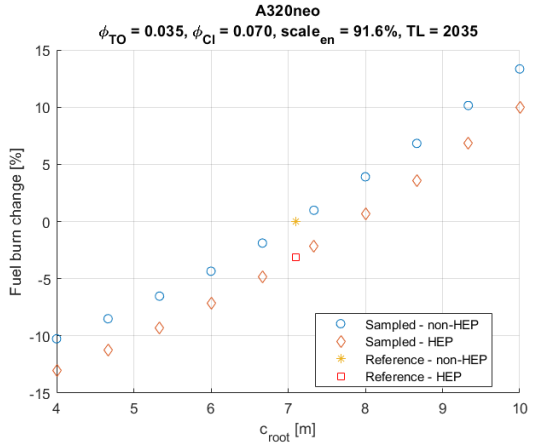

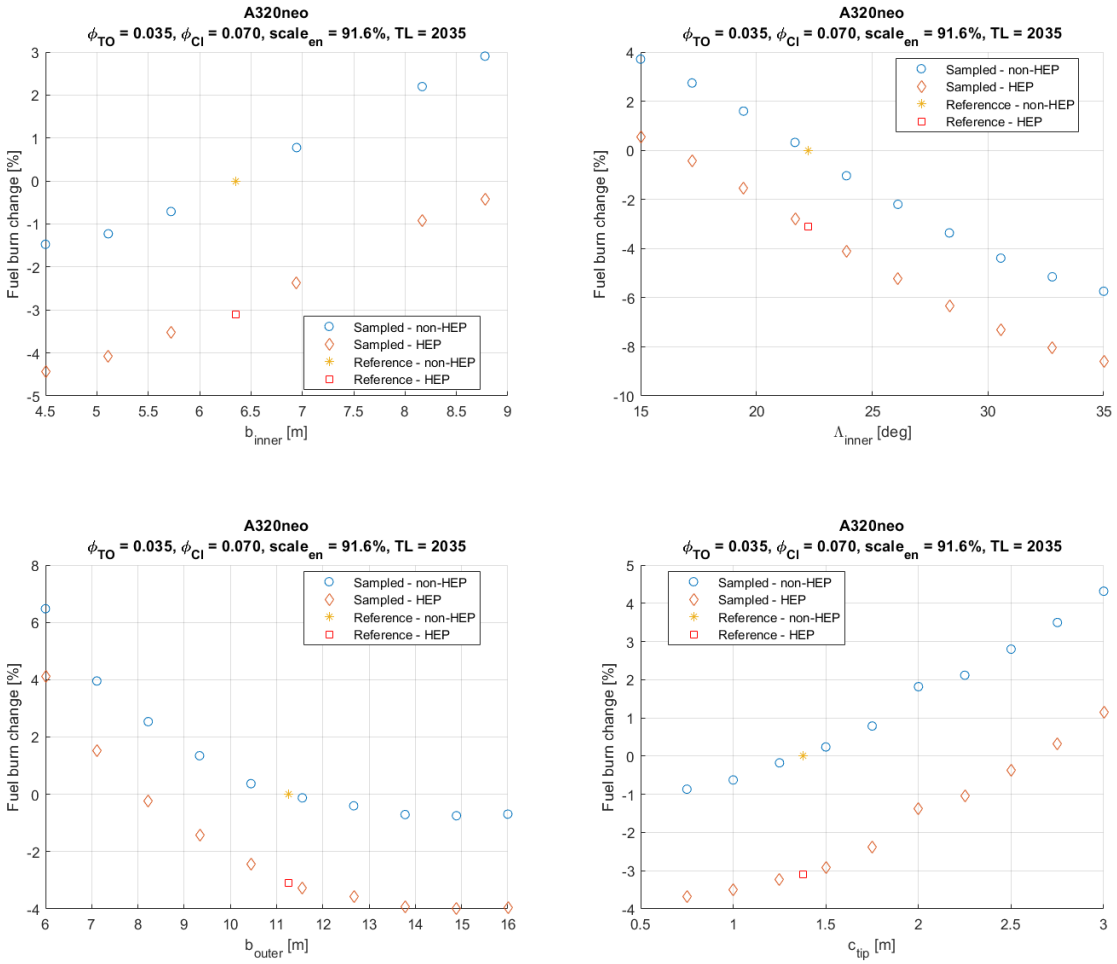

Figure B.1: The changes of fuel burn for the A320neo's design variables.

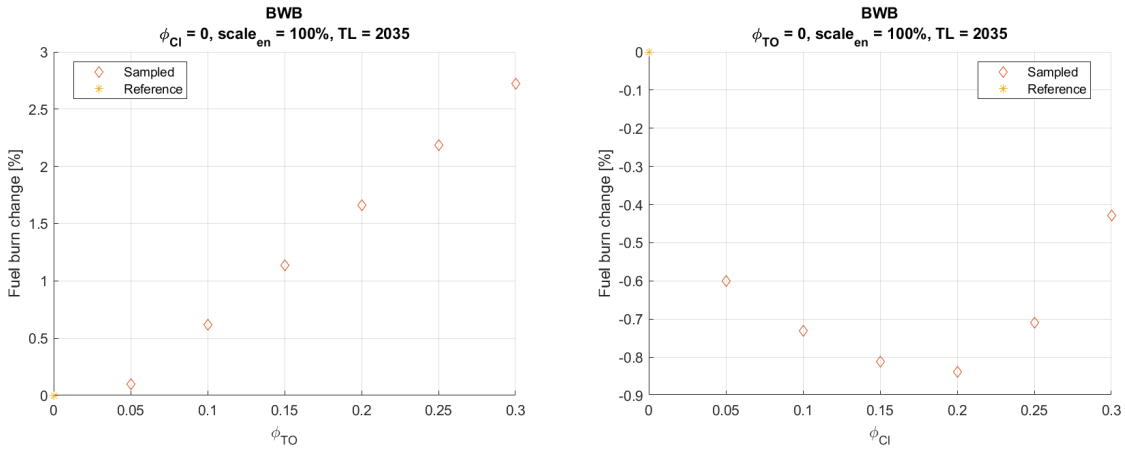

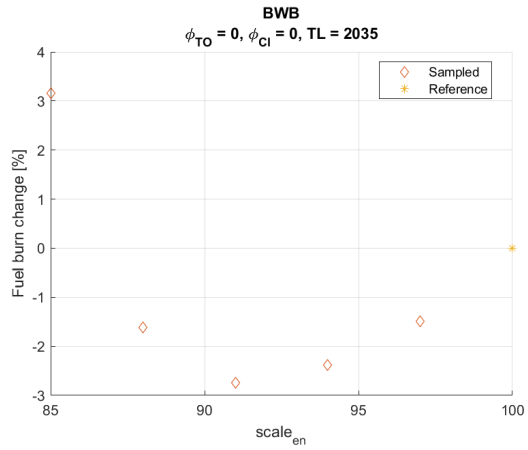
BWB
ϕ_{TO} = 0, ϕ_{CI} = 0, TL = 2035
Sampled
Reference
Fuel burn change [%]
scale$_{en}$

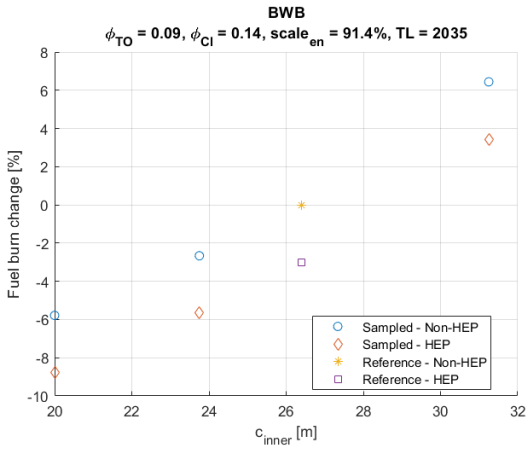
BWB
ϕ_{TO} = 0.09, ϕ_{CI} = 0.14, scale$_{en}$ = 91.4%, TL = 2035
Sampled - Non-HEP
Sampled - HEP
Reference - Non-HEP
Reference - HEP
Fuel burn change [%]
c$_{inner}$ [m]

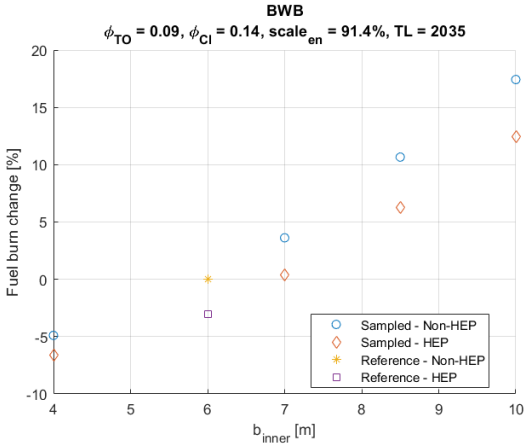
BWB
ϕ_{TO} = 0.09, ϕ_{CI} = 0.14, scale$_{en}$ = 91.4%, TL = 2035
Sampled - Non-HEP
Sampled - HEP
Reference - Non-HEP
Reference - HEP
Fuel burn change [%]
b$_{inner}$ [m]

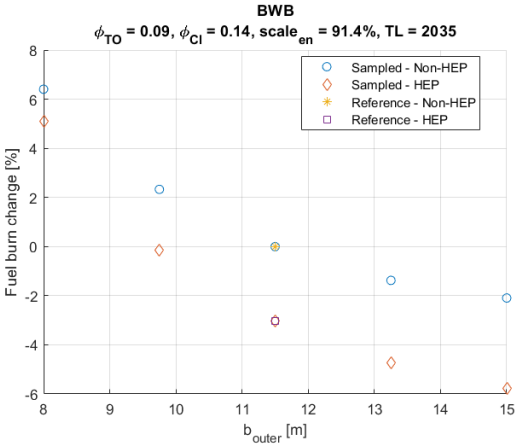
BWB
ϕ_{TO} = 0.09, ϕ_{CI} = 0.14, scale$_{en}$ = 91.4%, TL = 2035
Sampled - Non-HEP
Sampled - HEP
Reference - Non-HEP
Reference - HEP
Fuel burn change [%]
b$_{outer}$ [m]

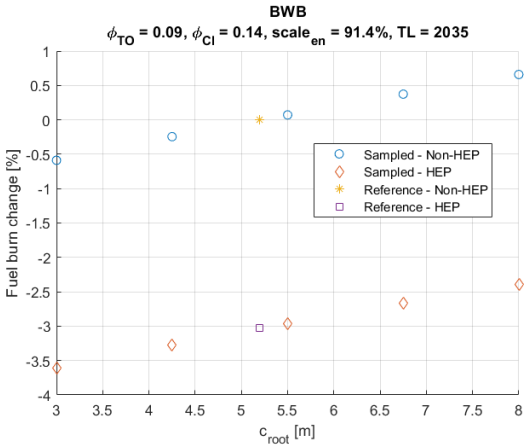
BWB
ϕ_{TO} = 0.09, ϕ_{CI} = 0.14, scale$_{en}$ = 91.4%, TL = 2035
Sampled - Non-HEP
Sampled - HEP
Reference - Non-HEP
Reference - HEP
Fuel burn change [%]
c$_{root}$ [m]

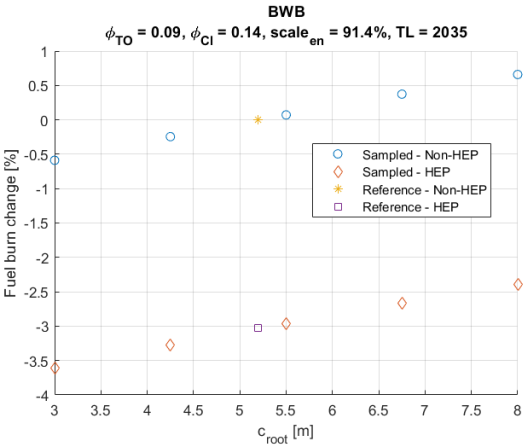
BWB
ϕ_{TO} = 0.09, ϕ_{CI} = 0.14, scale$_{en}$ = 91.4%, TL = 2035
Sampled - Non-HEP
Sampled - HEP
Reference - Non-HEP
Reference - HEP
Fuel burn change [%]
c$_{root}$ [m]

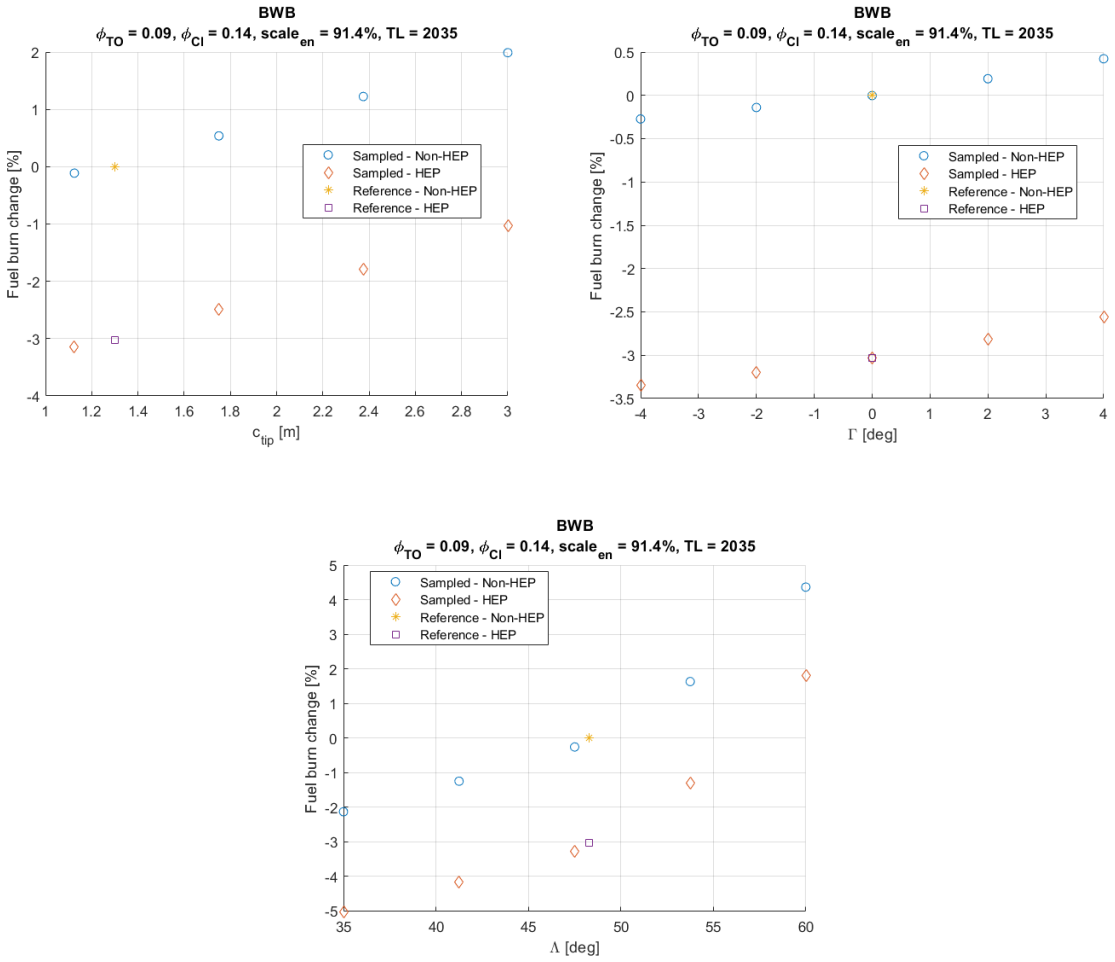

Figure B.2: The changes of fuel burn for the BWB's design variables.